magnetochemistry

MDPI

Article

NiFe Alloy Nanoparticles Tuning the Structure, Magnetism, and Application for Oxygen Evolution Reaction Catalysis

Rafael A. Raimundo [1,2], Vinícius D. Silva [3], Luciena S. Ferreira [3], Francisco J. A. Loureiro [4], Duncan P. Fagg [4], Daniel A. Macedo [3], Uílame U. Gomes [5], Márcio M. Soares [2], Rodinei M. Gomes [1] and Marco A. Morales [6,*]

1 Department of Mechanical Engineering, Universidade Federal da Paraíba, João Pessoa 58051-900, Brazil; rar@academico.ufpb.br (R.A.R.); rodineix@gmail.com (R.M.G.)
2 Department of Physics, Universidade Federal da Paraíba, João Pessoa 58051-900, Brazil; marciosoaresm@gmail.com
3 Department of Materials Science and Engineering, Universidade Federal da Paraíba, João Pessoa 58051-900, Brazil; viniciusdiasbrasil@hotmail.com (V.D.S.); luciena.ferreira@yahoo.com.br (L.S.F.); damaced@gmail.com (D.A.M.)
4 Centre for Mechanical Technology and Automation, Department of Mechanical Engineering, University of Aveiro, 3810-193 Averio, Portugal; francisco.loureiro@ua.pt (F.J.A.L.); duncan@ua.pt (D.P.F.)
5 Department of Materials Science and Engineering, Universidade Federal do Rio Grande do Norte, Natal 59078-970, Brazil; umbelino@fisica.ufrn.br
6 Department of Physics, Universidade Federal do Rio Grande do Norte, Natal 59078-970, Brazil
* Correspondence: morales@fisica.ufrn.br

Abstract: In this study, Ni-Fe alloy nanoparticles were prepared using the proteic sol–gel method, followed by a reduction in H_2 at 500 and 700 °C, namely hereafter as NiFe-500 and NiFe-700, respectively. The morphological, structural, and magnetic properties were tuned via the thermal treatment in H_2. The samples were studied using XPS, TEM, Mössbauer spectroscopy, DC magnetic measurements, and electrochemical measurements. Ritveld refinements showed that the sample NiFe-500 has FCC (face-centered cubic) and BCC (body-centered cubic) NiFe alloys, while the sample NiFe-700 has only FCC NiFe alloy. For both samples, magnetization measurements in the range of 300–900 K showed the presence of the Griffiths phase, indicating the formation of clusters of either Fe or Ni-Fe alloys rich in Fe. The sample NiFe-500 presented ferromagnetic (FM) transitions at 533, 700, and 834 K, assigned to the alloys $Ni_{37}Fe_{63}$-FCC, $Ni_{46}Fe_{54}$-FCC, and $Ni_{55}Fe_{45}$-FCC, respectively. In contrast, we could not observe the FM transition of the BCC Ni-Fe alloy because of limitations in our experimental setup ($T \leq 900$ K). Meanwhile, three FM transitions were observed for the sample NiFe-700 at 480, 655, and 825 K, attributed to the alloys $Ni_{34}Fe_{66}$-FCC, $Ni_{43}Fe_{57}$-FCC, and $Ni_{54}Fe_{46}$-FCC, respectively. At 5 K, the samples NiFe-500 and NiFe-700 have saturation magnetizations of 164.2 and 173.6 emu g^{-1}, respectively. For application in Oxygen Evolution Reaction catalysis, the samples NiFe-500 and NiFe-700 showed different overpotentials of 319 and 307 mV at 10 mA cm^{-2}. These low overpotential values indicate a higher electrochemical activity of the FCC Ni-Fe alloy and, for both samples, a superior electrocatalytic activity in comparison to RuO_2 e IrO_2 conventional catalysts. Furthermore, the samples showed high electrochemical stability in chrono potentiometric studies for up to 15 h. This current work highlights that the Ni-Fe alloys produced via the proteic sol–gel and with a reduction in H_2 methods can be promising for OER systems due to their good performance and low costs.

Keywords: nickel–iron alloy; magnetic properties; oxygen evolution reaction

Citation: Raimundo, R.A.; Silva, V.D.; Ferreira, L.S.; Loureiro, F.J.A.; Fagg, D.P.; Macedo, D.A.; Gomes, U.U.; Soares, M.M.; Gomes, R.M.; Morales, M.A. NiFe Alloy Nanoparticles Tuning the Structure, Magnetism, and Application for Oxygen Evolution Reaction Catalysis. *Magnetochemistry* **2023**, *9*, 201. https://doi.org/10.3390/magnetochemistry9080201

Academic Editors: Paula Corte-Leon and Ahmed Talaat

Received: 26 June 2023
Revised: 3 August 2023
Accepted: 4 August 2023
Published: 8 August 2023

1. Introduction

There is a growing interest in Ni-Fe (face-centered cubic, FCC) nanoalloys due to their unique structures and properties, including high magnetic permeability, high Curie temperature, high saturation magnetization, and good electrical conductivity [1–5]. These nanomaterials find applications in biomedicine as therapeutic and diagnostic agents [6,7],

catalytic agents [8], energy storage [9], electromagnetic wave absorbers [10], and sensors [11] with Ni-Fe alloys, with about 10–90 at.% iron being the most frequently used compositions [12]. The $Ni_{80}Fe_{20}$ (permalloy) and the $Ni_{45}Fe_{55}$ (elinvar) compositions are used in magnetic shielding, actuators, and magnetic motors [13]. Invar alloys, particularly the $Ni_{36}Fe_{64}$ composition, have been extensively explored in research because they have nearly zero thermal expansion over a wide temperature range and, thus, are applied to large cryogenic liquid containers and high-definition color displays [12]. Alloys with nickel concentrations above 30 at.% are the most versatile among soft magnetic materials and are used in electromagnetic applications. Below 30 at.% Ni, these alloys have an antiferromagnetic FCC structure with relatively low Néel temperature. Alloys with nickel contents close to 80 at.% have high magnetic permeability, while the maximum values of saturation magnetization and electrical resistivity are observed at 50 at.% and 30 at.% nickel [14].

Due to this versatility, Ni-Fe nanoparticles with specific morphologies and rigorous composition and structure control have gained increasing attention [15]. The literature reports the synthesis of Ni-Fe alloys via polyol reduction [16], vacuum induction melting [17], chemical precipitation [18], powder metallurgy [19], hydrothermal synthesis [20], selective laser melting [21], sol–gel [22], gas phase condensation [23], electroplating [24], solution blow spinning [25], electrospinning [26], among others. Among the aforementioned techniques, obtaining Ni-Fe alloys via chemical reduction (under a hydrogen atmosphere) of spinel-type ferrites ($NiFe_2O_4$) is a relatively simple preparation route that requires low processing temperatures. The production of metal alloys through the reduction of cobalt [27] and nickel [22] ferrites, as well as strontium [28,29] and barium [30] hexaferrites, have been widely investigated. Lima et al. [31] reported on the production of Ni-Fe alloys by reducing Ni ferrite, resulting in the tetraenite phase with Curie temperature (Tc) very close to the meteoric tetrataenite sample. Sun et al. [22] studied the structure and magnetic properties of Ni_xFe_{3-x} (x = 0; 0.5; 1; 1.5) prepared using sol–gel method, achieving a high magnetic moment for alloys with x = 0.5 and 1.5. Azizi et al. [8,32] synthesized Ni-Fe and Ni-Co-Fe alloys by reducing Ni ferrite and Ni-Co ferrite, respectively, obtaining the following results: (a) metal alloy aggregates with micrometer sizes; (b) saturation magnetization (Ms) of 45.9 and 42.9 emu g^{-1}; (c) coercivity field (Hc) of 69.2 Oe and 116.2 Oe; and (d) remanent magnetization (Mr) of 3.4 and 2.7 emu g^{-1}.

From the point of view of energy sustainability, metal alloys are promising candidates for the oxygen evolution reaction (OER, $4OH^-(aq) \rightleftharpoons 2H_2O(l) + O_2(g) + 4e^-$), which features in energy conversion and storage technologies, such as metal–air batteries, fuel cells, and electrolysis cells [33]. In particular, the NiFe alloy has generated interest due to its excellent performance as an OER electrocatalyst in an alkaline medium, presenting high efficiency and stability, high resistance to chemical/mechanical degradation, and low overpotential (η) at a reference current density of 10 mA cm^{-2} [34].

Metal alloy nanomaterials, in general, can crystallize in the most diverse forms: hexagonal close-packed (HCP), face-centered cubic (FCC), body-centered cubic (BCC), and face-centered tetragonal (FCT) [35]. Each type of crystal structure has unique electronic properties that directly influence catalytic activity. Therefore, the choice (selectivity) of the crystal structure that presents a high proportion of exposed facets can be a strategy to improve the catalytic performance [36–38]. In fact, some works have already been carried out to study the effect of the crystal structure (FCC, HCP, FCT) on electrocatalytic properties. For example, NiFe alloy nanoparticles with HCP crystalline structure have superior catalytic activity for OER compared to their FCC counterparts [37], while FePt nanoparticles with the FCT phase have a higher activity and durability than the FCC phase for the oxygen reduction reaction (ORR) [39].

The performance of electrocatalysts can also be improved by controlling the composition of the alloy. According to Vo et al. [40], the increase in nickel content in Ni_xFe_{100-x} alloys (x = 0, 25, 50, 75, and 100), prepared using controllable film electrodeposition, leads to a reduction in their overpotential values, e.g., the alloys $Ni_{75}Fe_{25}$, $Ni_{50}Fe_{50}$, and $Ni_{25}Fe_{75}$ exhibit over-potentials of 316, 321, and 361 mV, respectively.

The review written by Jamesh Mohammed-Ibrahim [34] reports that the structure–activity relationship of NiFe-based materials plays a crucial role in the generation of active sites with ideal bonding energy, thus, decreasing the energy barrier for OER. Therefore, designing catalysts with an appropriate electronic structure is one of the great challenges found in this field. Recently, our group reported the production of NiFe-$NiFe_2O_4$ fibers by solution blow spinning with excellent chemical stability, low overpotential (η = 316 mV vs. RHE at 10 mA cm^{-2}), and an impressive turnover frequency (TOF) of 4.03 s^{-1} for an overpotential of 400 mV [25]. Y. Liang et al. [41] reported the first use of commercial NiFe foam, achieving stable catalytic activity for up to 10 h and an overpotential of 320 mV at 10 mA cm^{-2}. M. Biset-Peiró et al. [42] produced uniform films via sequential and alternative thermal evaporation of Ni and Fe and recorded an overpotential of 370 mV at 10 mA cm^{-2}.

The aim of the current research is to study (i) the effectiveness of the proteic sol–gel method [43–45] in producing magnetic single-domain nickel ferrite nanoparticles, (ii) to tune the structural, chemical, and magnetic properties through the reduction process for the synthesis of the NiFe alloy, and (iii) the application of the NiFe alloys as electrocatalysts for oxygen evolution reaction (OER) in alkaline media.

2. Materials and Methods

Nickel nitrate hexahydrated ($Ni(NO_3)_2.6H_2O$, Dinâmica Ltd., Brazil, iron nitrate nonahydrated ($Fe(NO_3)_3.9H_2O$, Sigma Aldrich, Brazil), flavorless gelatin (Dr. Oetker, Brazil), methanol (99%, Vetec, Brazil), Nafion® solution 5 wt% (Sigma Aldrich, Brazil), isopropanol (99%, Vetec, Brazil), and commercial Ni foam (Ni 99.8%, porosity > 95%, QiJing Ltd., Ningbo, China) were used as starting materials.

2.1. Preparation of $NiFe_2O_4$ Powders and NiFe Alloys

$Ni(NO_3)_2.6H_2O$, $Fe(NO_3)_3.9H_2O$, and gelatin were used to synthesize $NiFe_2O_4$. Initially, 2.0 g of gelatin was dissolved in 50 mL of distilled water at 70 °C. Subsequently, 2.477 g of nickel nitrate and 6.894 g of iron nitrate were added (Ni/Fe molar proportion of 1:2), and the final solution was stirred at 90 °C until evaporation of water and formation of a gel. The precursor was treated at 800 °C for 2 h in the presence of air. Then, the nickel ferrite powder was thermally treated for 2 h under H_2 flux at 500 °C (NiFe-500) and 700 °C (NiFe-700). The chemically reduced samples were cooled to room temperature in presence of flowing H_2 gas. Figure 1 shows the schematic representation of the fabrication process of the NiFe alloy nanoparticles. Immediately after production, the reduced samples were enclosed in Argon gas to prevent oxidation.

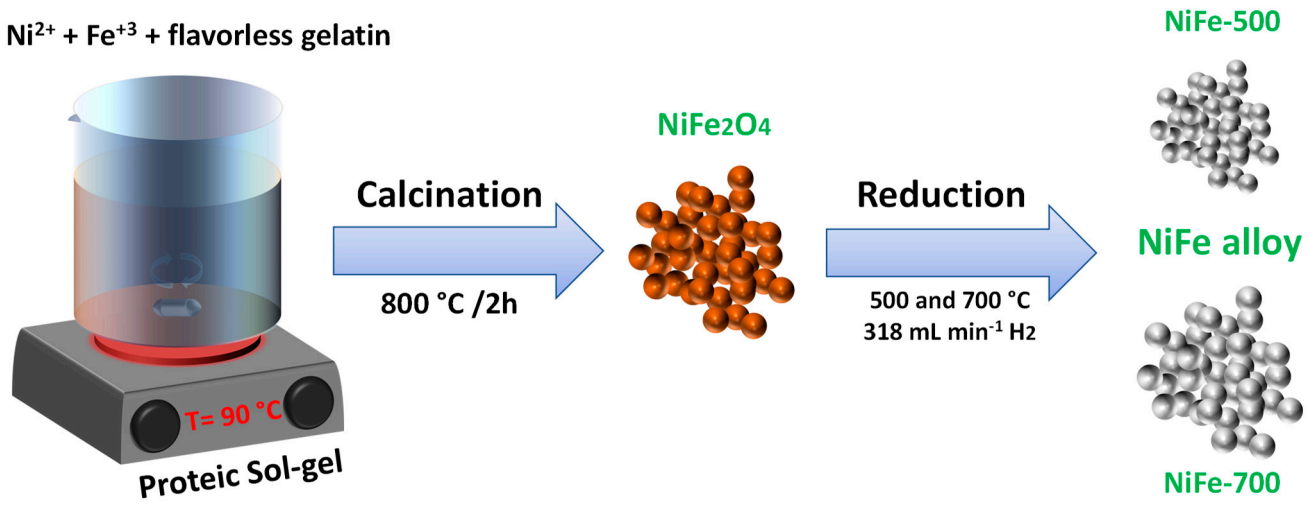

Figure 1. Schematic representation of the fabrication process for the NiFe oxide and NiFe alloy nanoparticles.

2.2. Structural, Morphological, Chemical, Mössbauer, and Magnetic Characterization

Morphology and particle sizes were determined with a scanning electron microscope (Carl Zeiss, Supra 35-VP, USA) equipped with a Bruker EDS detector (XFlash 410-M, USA). To assess the sample's morphology, transmission electron microscopy (TEM) images were obtained using a commercial microscope (JEOL, JEM-2100, USA). The software ImageJ (National Institutes of Health, USA) [46] was applied to determine the distribution of particle sizes after analysis of 300 particles. The crystalline structure was studied via X-ray diffractometry (Miniflex II, Rigaku, Japan) using monochromatic Cu (Kα, λ = 1.5418 Å) radiation. The data were recorded in the 2θ range from 10° to 80°, with step sizes of 0.02°. The vibrational modes were studied in an infrared spectrometer (IRPrestige-21, Shimadzu, Japan). The crystallite sizes and lattice parameters were determined via Rietveld refinement of the X-ray data using the software TOPAS [47]. The chemical nature of the sample's surface was studied using X-ray photoelectron spectroscopy (XPS). The measurement was carried out in an ultrahigh vacuum system with a base pressure of 2×10^{-10} mbar located at TEMA, University of Aveiro (Portugal), using a SPECS Phoibos 150 (Japan) spectrometer with a high-intensity monochromatic Al Kα X-ray source (1486.6 eV). High-resolution spectra were recorded at normal emission take-off angle and with a pass-energy of 20 eV, providing an overall instrumental peak broadening of 0.5 eV. The binding energy was referenced to C 1s line at 284.5 eV for calibration. Using XPSPEAK 4.1 fitting software, the height, area, and position of the peaks were determined by allying the separation of measured XPS spectra. The Mössbauer spectra were recorded at 300 K using a spectrometer from SEECO with a 57Co: Rh radioactive source with 20 mCi activity. The data were fit using the software NORMOS90 [48]. The isomer shifts are relative to α-Fe at 300 K. The magnetic measurements as a function of magnetic field and temperature (M-H and M-T) were performed using a physical properties measurement system (PPMS-Dynaccol, Quantum Design, USA) equipped with a vibrating sample magnetometer (VSM). The M-H measurements were recorded at 5 K under a maximum field of 10 T. The M-T measurements were recorded from 300 K to 900 K under a magnetic field of 160 Oe.

2.3. Electrode Preparation and Electrochemical Characterization

The electrochemical OER activity of NiFe samples was evaluated using a Metrohm Autolab PGSTAT204-FRA32 M (USA) in a three-electrode system with an alkaline KOH solution (1 M, pH = 13.58 $\pm$ 0.03) at 25 °C. Platinum wire and Ag/AgCl (3 M KCl) were used as counter and reference electrodes, respectively. The working electrode was prepared by depositing the catalytic ink under a substrate (nickel foam). Before the deposition process, the Ni foam substrate was cleaned via sonication in 6 M HCl, then in acetone, and finally in deionized water, each process in periods of 10 min. The catalytic inks were prepared with 5 mg of the catalyst (NiFe-500 and NiFe 700) and 20 µL of 5% Nafion, being subsequently mixed in 500 µL of isopropanol and sonicated for 10 min to prepare an ink with suitable dispersion. Then, the inks were deposited on Ni substrates (1 cm $\times$ 1 cm) and dried at room temperature for 5 h.

All potential values (corrected for iR) were converted to that corresponding to the reversible hydrogen electrode (RHE) using the Nernst equation (Equation (1)), while the values of overpotential (η) were calculated using Equation (2). The linear sweep voltammetry (LSV) was verified at 5 mV s^{-1} in the potential range of 0.1 at 1.5 V. Electrochemical impedance spectroscopy (EIS) was performed using the frequency range of 0.1 Hz to 10 kHz, under applied DC potential (1.6 V vs. RHE) and voltage amplitude of 5 mV. Chronopotentiometry experiments for 15 h at 10 mA cm^{-2} were performed to verify long-term stability.

$$\mathrm{ERHE} = \mathrm{EAg/AgCl} + 0.059 \times \mathrm{pH} + 0.1976 \quad (1)$$

$$\eta = \mathrm{ERHE} - 1.23\ \mathrm{V} \quad (2)$$

3. Results and Discussion

3.1. Characterization of $NiFe_2O_4$ Produced by Proteic Sol–Gel Synthesis

FESEM, particle size distribution, FT-IR, and X-ray diffraction (XRD) results of the nickel ferrite powder synthesized using the proteic sol–gel method are shown in Figure 2. The FESEM image (Figure 2a) was expanded to provide more visible characteristics of the microstructural and morphological properties of $NiFe_2O_4$, The size distribution was obtained after analyzing more than 300 nanoparticles, we noticed a quasi-spherical morphology with a mean diameter of 40 nm (Figure 2b). The formation of the spinel structure ($NiFe_2O_4$) is also suggested by the FT-IR results (Figure 2c) from the observation of the cation-oxygen band at 590 cm^{-1} that can be attributed to the stretching vibration of the tetrahedron Fe-O specie. Three further broad bands is observed at 1650 cm^{-1}, 2300 cm^{-1}, and 3380 cm^{-1} and are attributed to H-O-H vibrations due to absorbed/free water. The 1130 cm^{-1} band may be ascribed to traces of nitrate ions. Finally, a single band observed near 3000 cm^{-1} is associated with the C-H stretching. The refined XRD pattern (Figure 2d) confirms the presence of a single phase with diffraction peaks that are characteristic of the spinel-type crystal structure of $NiFe_2O_4$ (ICSD card n° 40040, space group Fd-3mS, 227, lattice parameter a = 8.33 Å) [49]. Eleven diffraction peaks are observed at positions 2θ = {30.2°; 35.6°; 37.2°; 43.3°; 53.7°; 57.3°; 62.9°; 71.4°; 74.5°; 75.5°; and 79.54°} indexed to Miller indexes (110), (200), (211), (110), (200), (211), (110), (200), (211), (110), and (200), respectively. The refined lattice parameter of $NiFe_2O_4$ is 8.337 Å, in accordance with that previously reported [49]. The agreement parameters Rwp and Rexp were 2.38% and 0.91%, respectively. The value χ^2 = 2.61 suggests a good fit between the experimental and calculated model. The $NiFe_2O_4$ powder had a crystallite size of 39 nm, which is in good agreement with the particle size (40 nm) obtained using FESEM. Based on these results, proteic sol–gel synthesis is shown to be an efficient chemical approach for obtaining high-purity monodisperse powder particles.

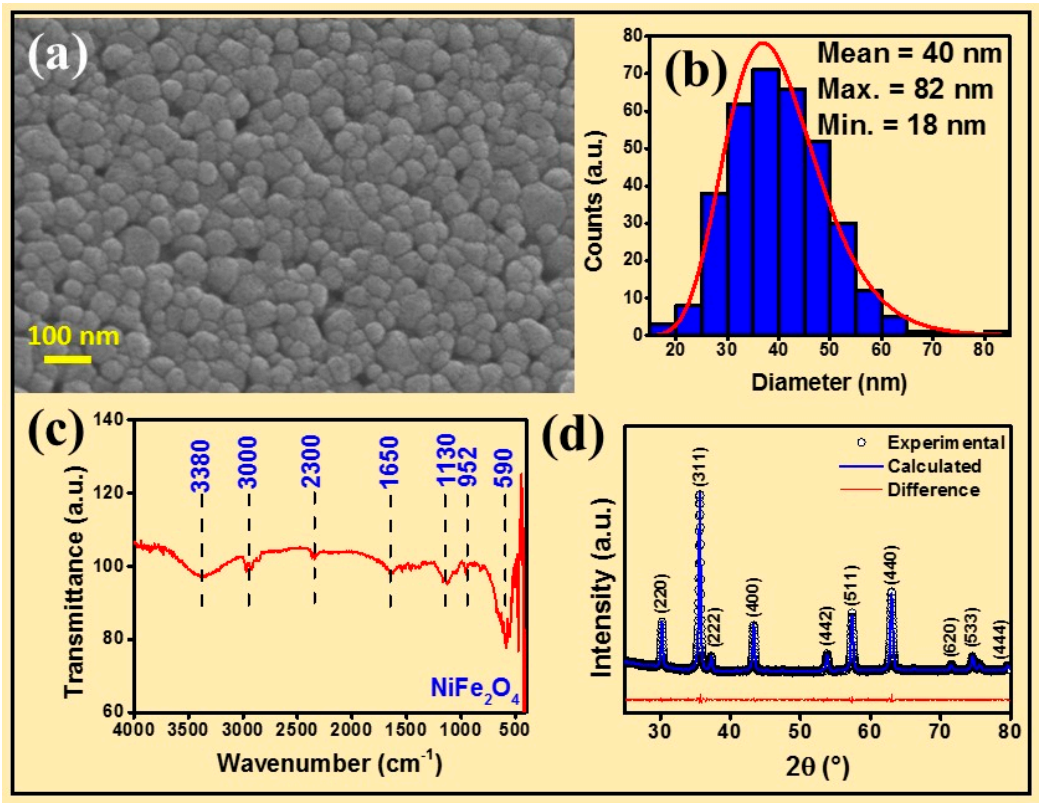

Figure 2. (**a**) FESEM image, (**b**) particle size distribution, (**c**) FTIR spectrum, and (**d**) refined XRD pattern of nickel ferrite synthesized via proteic sol–gel method.

3.2. Structural, Morphological, and Chemical Characterization

The diffraction patterns of the Ni-Fe alloys produced via chemical reduction under the H_2 atmosphere are shown in Figure 3. The samples have well-defined and intense diffraction peaks, with a small width at half height. The peaks observed in the diffraction experiments are associated with the crystalline phases of solid solutions of Ni on the base of γ-Fe (FCC, cubic, structure of the type fcc(ccp)-Cu) and α-Fe (BCC, cubic, structure of the type bcc-W). The sample NiFe-500 shows a biphasic crystalline structure (FCC and BCC), while the sample NiFe-700 shows a single FCC crystalline structure. The diffraction peaks of the FCC phase are related to crystalline planes (111), (200), and (220), being located at 2θ = {43.57°, 50.87°, and 74.61°}, while the BCC phase shows peaks indexed to crystalline planes (110), (200), and (211) observed at positions 2θ = {44.62°, 64.95°, and 82.20°}, respectively. Additional phases due to oxides are not detected, showing that the chemical reduction process was successfully performed.

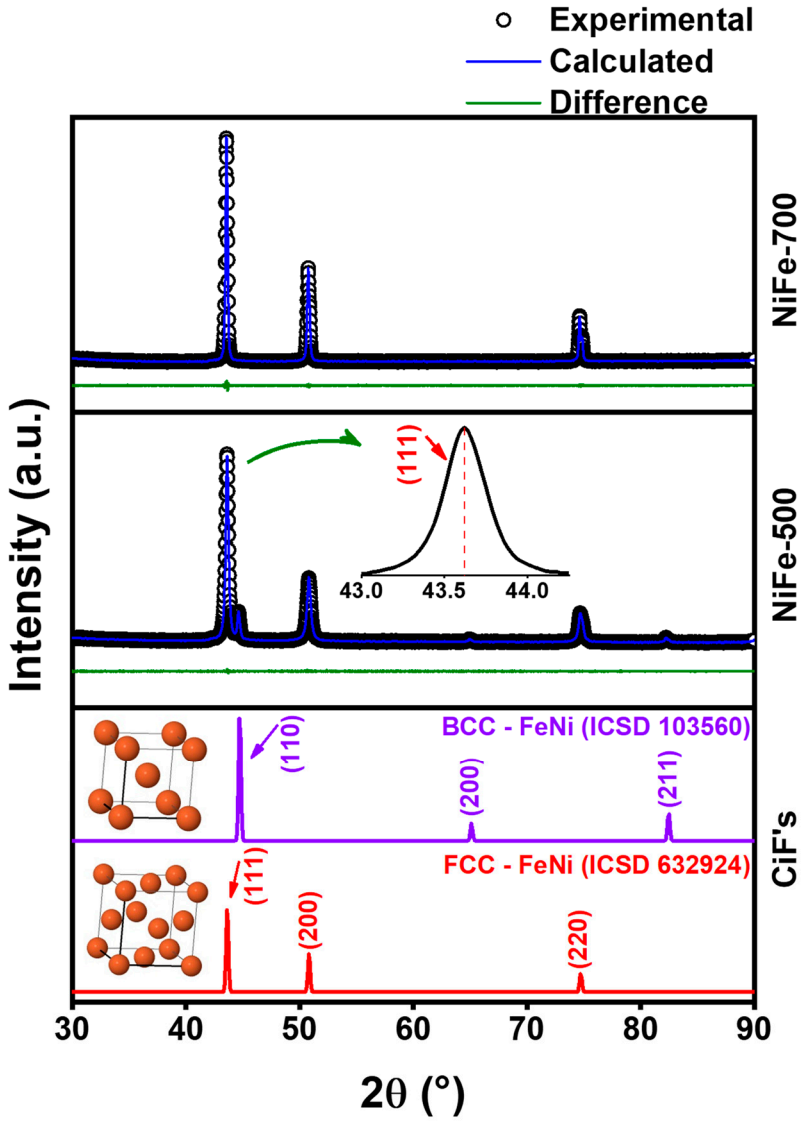

Figure 3. XRD patterns of the Fe-Ni alloys obtained from the reduction of Ni ferrite under H_2 atmosphere at temperatures of 500 °C (NiFe-500) and 700 °C (NiFe-700). Simulated XRD patterns (according to CIF files) used to refine the diffractograms are also shown.

The samples were refined using the Rietveld method, with card files (ICSD database) of the phases $Ni_{34}Fe_{66}$-FCC (a = 3.5928 Å, ICSD n° 632924, Fm-3m (225)) [50] and NiFe-BCC

Fe-rich alloy (a = 2.8650 Å, ICSD n° 103560, Im-3m (229)) [51]. Figure 3 shows that the sample NiFe-700 is a single FCC phase, and the sample NiFe-500 is biphasic with FCC and BCC NiFe alloys. The sample NiFe-500 has the same phases as the NiFe alloy produced by Lim et al. [52] in a two-stage synthesis: (i) the production of $NiFe_2O_4$ via hydrothermal synthesis at 200 °C for 12 h and (ii) the subsequent reduction at 500 °C for 5 h in a mixed atmosphere of 10% H_2/90% Ar. The simulation of XRD peaks using the CIF cards is also shown in Figure 3. The insert in Figure 3 shows only the peak (111) of the $Ni_{34}Fe_{66}$-FCC phase. We noticed that this peak is symmetric, indicating a homogeneous phase. However, we cannot rule out the presence of FCC alloys with crystallite sizes under 2–3 nm, below the detection limit of the XRD technique. The crystallite size, phase composition, lattice parameters (theoretical and calculated), and agreement factors are shown in Table 1. The lattice parameters of the $Ni_{34}Fe_{66}$-FCC and NiFe-BCC phases are in agreement with those reported in their respective ICSD cards. The maximum values of agreement factors Rwp (%) and Rexp (%) are found to be 3.95% and 3.22%, respectively. The obtained $\chi^2 \leq 1.23$ shows excellent agreement between experimental and refined models.

In both samples, the alloy $Ni_{34}Fe_{66}$-FCC is shown to be the dominant phase. The crystallite sizes of the FCC phase in samples NiFe-500 and NiFe-700 are 37 nm and 52 nm. The crystallite size of the NiFe-BCC phase present in the sample NiFe-500 is 60 nm. These results are in agreement with the phase diagram of Ni-Fe alloy for solid solutions, proposed by Swartzendruber et al. [53], J.J. Goldstein et al. [54], and O. Kubaschewsk [55]: (1) solid solution FCC (γFe, Ni) in a wide range of composition (20–100%wt. Ni) and (2) solid solution BCC in the iron-rich region (0–10%wt. Ni) at low temperature (αFe, T < 912 °C); highlights of this research. Our results agree well with other studies that have used alternative methods such as electrodeposition [12] and electrical explosion [56] to produce NiFe alloys with a biphasic structure (FCC/BCC) at low temperatures.

Table 1. XRD parameters obtained from Rietveld refinements. Numbers in brackets are relative concentrations.

Sample	NiFe-FCC (632924)		NiFe-BCC (103560)		Agreement Factors		
	D_{XRD} (nm)	a (Å)	D_{XRD} (nm)	a (Å)	R_{wp} (%)	R_{exp} (%)	χ^2
$Ni_{34}Fe_{66}$-(FCC)—ICSD 632924	---------	3.5928	---------	---------	---------	---------	---------
NiFe-(BCC)—ICSD 103560	---------	---------	---------	2.8650	---------	---------	---------
NiFe-500	37 [93 wt%]	3.5906	60 [7 wt%]	2.8685	4.26	3.78	1.13
NiFe-700	52 [100 wt%]	3.5912	---------	---------	3.95	3.22	1.23

FESEM images of Ni-Fe samples after the reduction process at 500 °C (NiFe-500) and 700 °C (NiFe-700) are shown in Figure 4. A detailed analysis of FESEM images allowed us to determine particle morphologies and size distribution. The micrographs show agglomerates composed of quasi-spherical grains (Figure 4a,g), indicating that the reduction process at high temperatures caused particle coalescence. Samples NiFe-500 (mean particle size of 72 nm) and NiFe-700 (mean particle size of 287 nm) had particle sizes varying from 31 to 140 nm and from 170 to 570 nm, respectively. Both samples have particle sizes larger than those of the Ni-ferrite precursor sample (Figure 2b). The spatial distribution of Ni and Fe metals in these materials is inspected via energy-dispersive X-Ray spectroscopy (EDS), as shown in Figure 4d–f,j–l. EDS mapping analysis indicates the high purity of Ni-Fe alloys with an atomic composition of $NiFe_2$ (i.e., $Ni_{34}Fe_{66}$). As observed, there is a homogenous distribution of red (Fe) and green (Ni) spots, indicating that these elements are homogeneously dispersed in the samples. Moreover, residual oxygen was not detected, indicating that the reduction process under H_2 flux was performed successfully. The composition of the alloys determined via EDS confirms the results obtained using XRD.

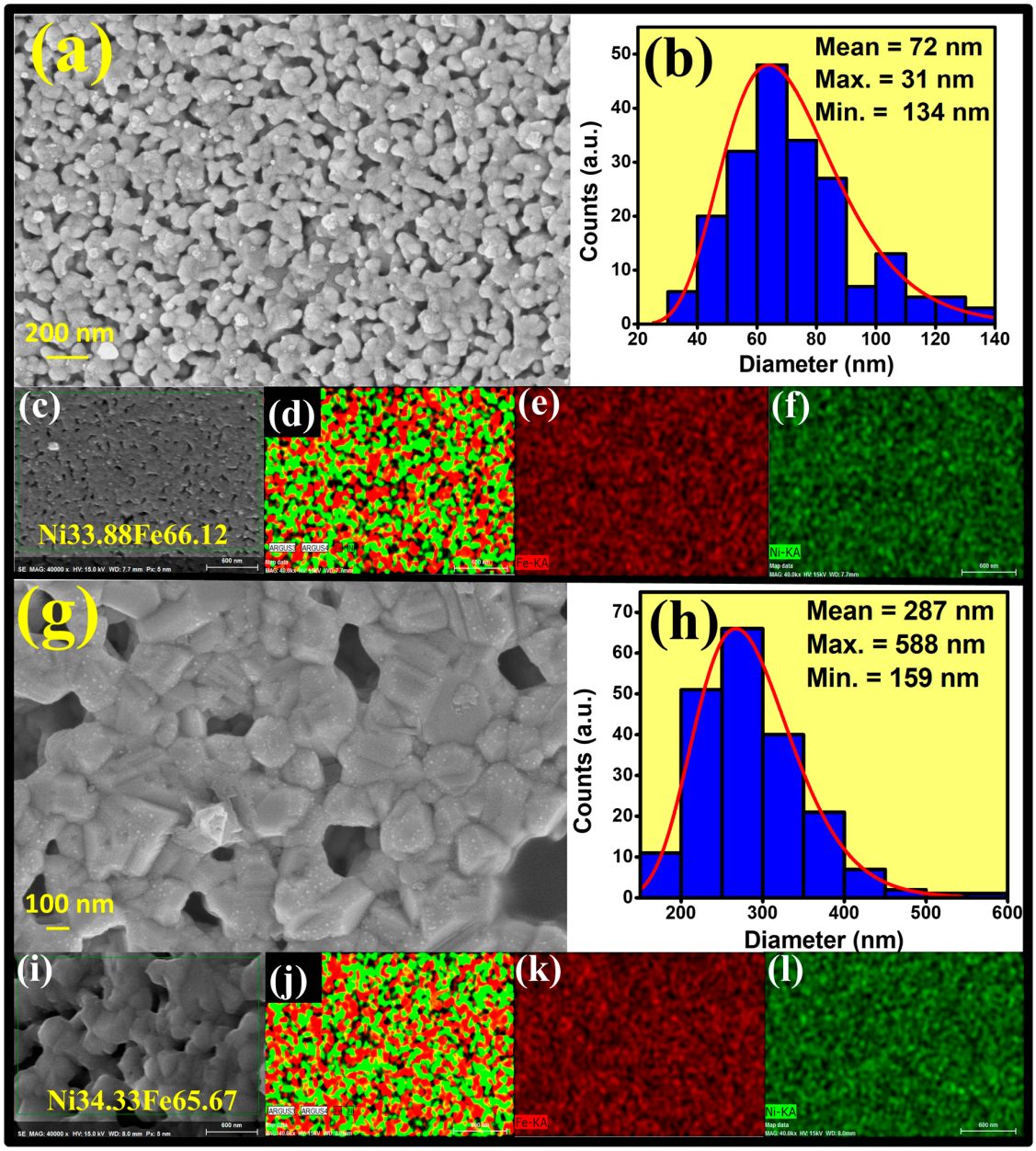

Figure 4. (**a**,**g**) FESEM images. (**b**,**h**) particle size distributions, the red line is the Lognormal fitting of the experimental data. (**d**–**f** and **j**–**l**) EDS mapping, red and green spots are due to Fe and Ni signals. Images (**a**–**f**) and (**g**–**l**) are for nanoparticles reduced at 500 °C (NiFe-500) and 700 °C (NiFe-700), respectively.

TEM images of NiFe-500 and NiFe-700 samples are shown in Figures 5a and 5b, respectively. Upon carefully inspecting the morphologies, we observed that the nanoparticles are quasi-spherical with varying diameters. In both samples, the nanoparticles form spherical aggregates. NiFe-500 (Figure 5c) and NiFe-700 (Figure 5d) samples have an average particle size of 61 and 164 nm, respectively, with size distributions ranging from 18.5 to 128 nm (Figure 5c) and 73 to 310 nm (Figure 5d), respectively. The particle sizes obtained from the TEM images (Figure 5c,d) differ slightly from that of the crystallite sizes obtained using XRD (Table 1). We believe that this divergence is related to the high degree of aggregation of the nanoparticles. The growth of bimetallic nanoparticles, as well as their structural and physical properties, are influenced by complex factors, such as temperature, total energy, and chemical ordering of Ni and Fe [15]. Figure 5g shows the SAED pattern of the biphasic sample NiFe-500, with diffraction rings originating from the crystalline planes of the NiFe-FCC phase marked in green [(111), (200), (220), (311), (440)] and those of the NiFe-

BCC phase marked in red [(211)]. Figure 5h shows the SAED pattern of the single-phase NiFe-700 sample with planes referring to the NiFe-FCC phase. These results confirm the crystallinity of NiFe nanoparticles. High-magnification TEM images (Figure 5e,f) reveal very thin fringes with an atomic spacing of 0.207 nm, referring to the NiFe plane (111).

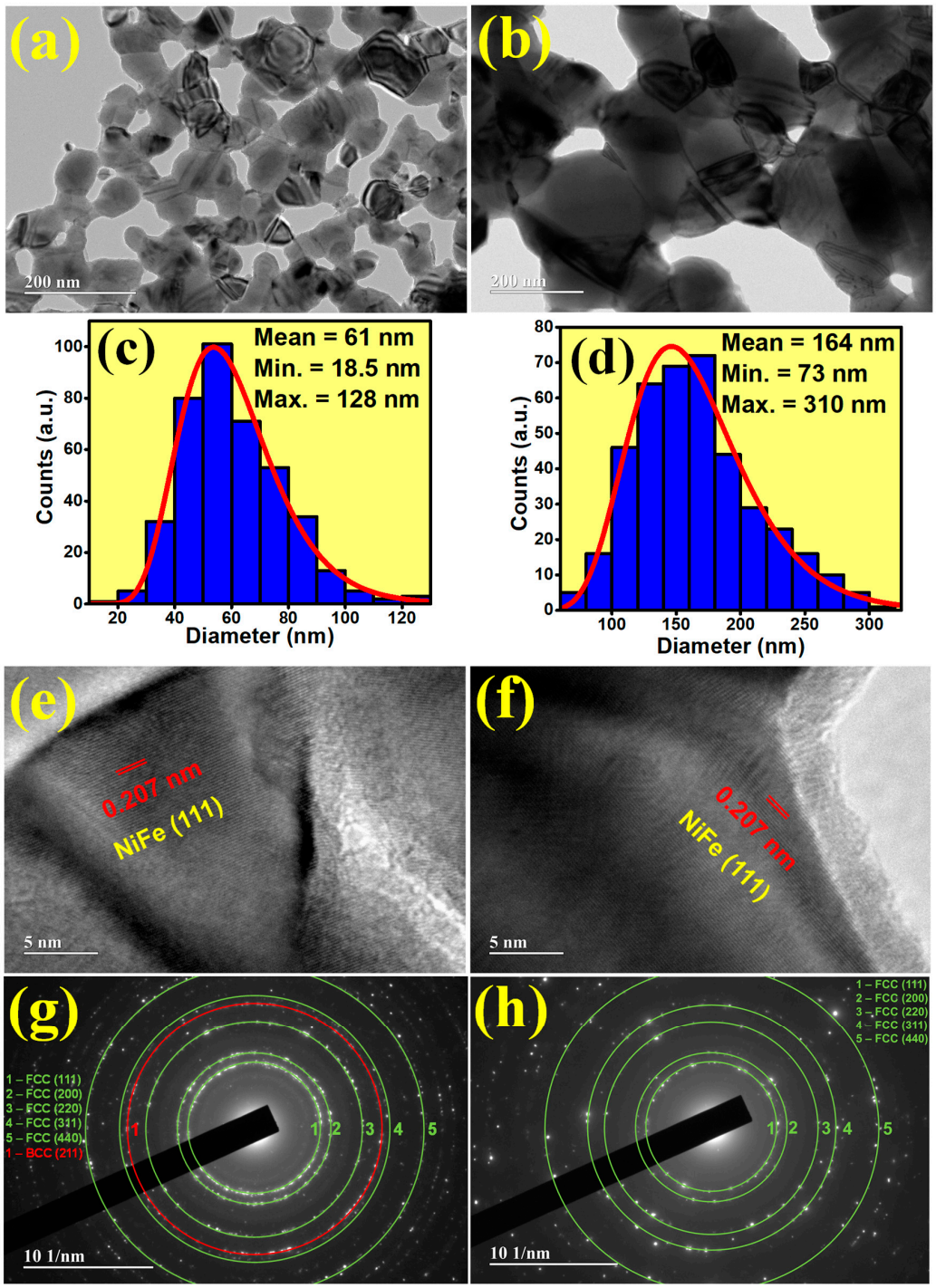

Figure 5. TEM, size distribution, and SAED patterns of NiFe alloys: (**a**,**c**,**e**,**g**) NiFe-500 and (**b**,**d**,**f**,**h**) NiFe-700. The red line is the Lognormal fitting of the experimental data.

X-ray photoelectron spectroscopy (XPS) was used to investigate the surface chemical composition and oxidation state of both NiFe-500 and NiFe-700 samples. Figure S1 presents the overview XPS spectra of both samples, covering the C 1s, the Ni 2p, the Fe 2p, and the O1s bands. Figure 6a,b depict the Ni ($2p_{3/2}$) XPS high-resolution spectra, where peak

deconvolution leads to the identification of the 2+ and 3+ oxidation states, at, respectively, 854.75 and 855.76 eV for the NiFe-500 sample; and 854.91 and 856.01 eV for the NiFe-700 sample, in line with previous works [57–60]. The presence of the redox couple Ni^{2+}/Ni^{3+} likely results from the partial oxidation of metallic Ni at the particle's surface. In this case, the presence of Ni^{2+} can be ascribed to the formation of NiO or $Ni(OH)_2$, which may be related to some adsorbed moisture, while further oxidation, related to Ni^{3+}, is also possible due to the formation of NiOOH, as previously suggested [61,62].

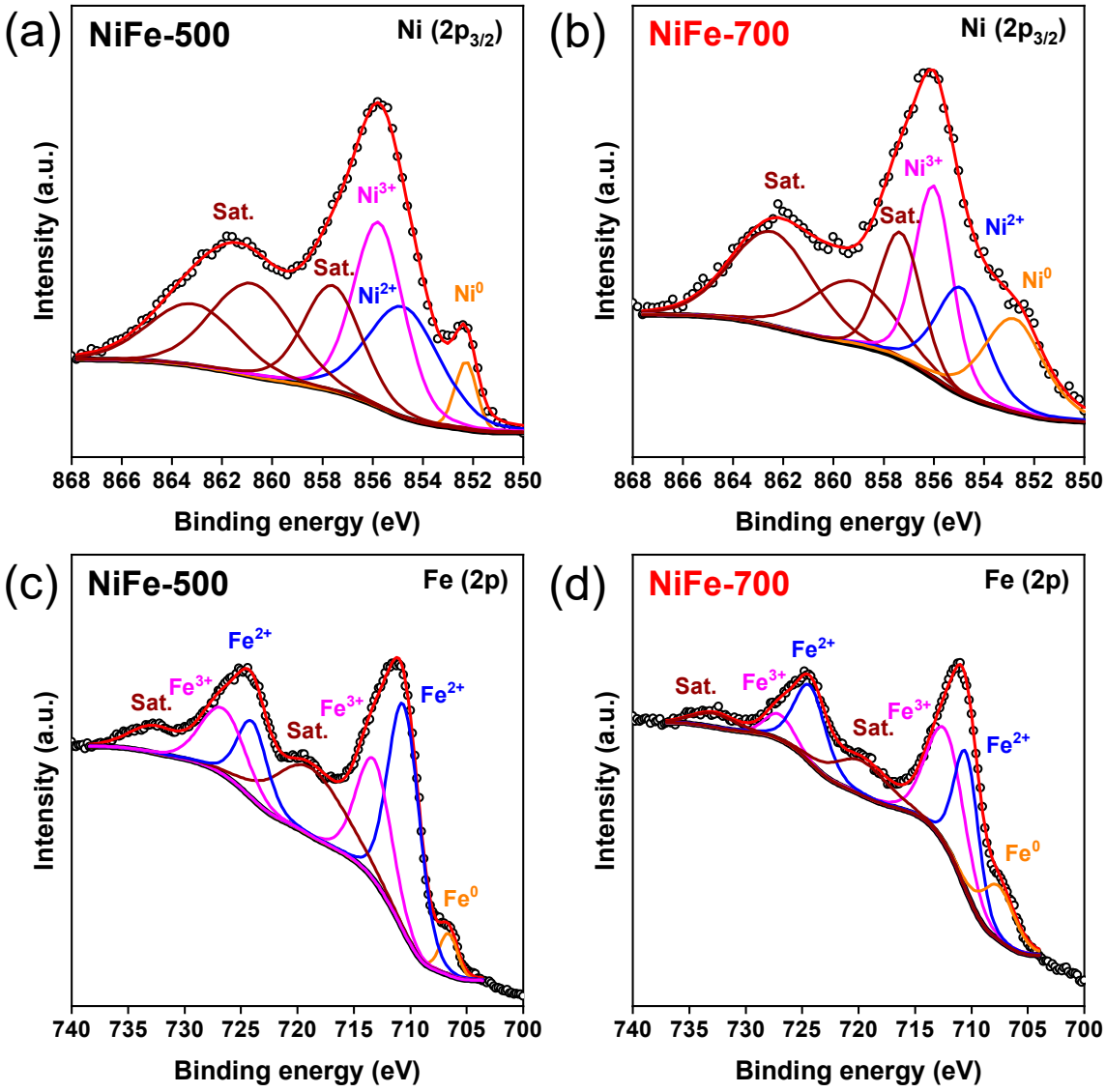

Figure 6. High-resolution XPS spectra of (**a**,**b**) Ni ($2p_{3/2}$) and (**c**,**d**) Fe (2p) of the NiFe alloys.

Nonetheless, a small peak related to metallic Ni^0, at 852.29 and 852.81 eV for both NiFe-500 and NiFe-700 samples, respectively, was also identified. Hence, for comparing the Ni reducibility, we have calculated the ratio between metallic and oxidized nickel, i.e., $[Ni^0]/([Ni^{2+}] + [Ni^{3+}])$, which was found to increase with increasing reducing temperature, i.e., from 0.07 to 0.31. Such behavior is expected due to the higher reducibility of Ni at higher temperatures, as predicted by the thermodynamic equilibrium $(Ni(s) + {}^1/_2O_2(g) \Leftrightarrow NiO(s))$ [63]. In addition, three satellite peaks were also deconvoluted at 857.59, 860.82, and 863.16 eV for the NiFe-500 sample and 857.34, 859.21, and 862.46 eV for the NiFe-700 sample.

Figure 6c,d depict the XPS high-resolution spectra of the Fe (2p) spectra of both NiFe-500 and NiFe-700 sample surfaces. In this case, both the $2p_{3/2}$ and $2p_{1/2}$ orbit spins were

used in the fitting procedure for facilitating the background calculation. The XPS spectra depict the metallic Fe^0 at 706.58 eV (NiFe-500) and 707.12 eV (NiFe-700). However, the presence of Fe^{2+} and Fe^{3+} at higher binding energies was also identified. In addition, the satellite peaks are present at 719.16 eV and 719.62 eV ($2p_{3/2}$) and at 732.42 eV (NiFe-500) and 732.97 eV (NiFe-700) ($2p_{1/2}$). Similar to that observed for Ni, the presence of Fe in higher oxidation states probably occurs due to the spontaneous oxidation of Fe on exposure to air atmosphere [64,65]. In addition, the ratio between metallic and oxidized iron, i.e., $[Fe^0]/([Fe^{2+}] + [Fe^{3+}])$, was also found to increase with increasing reducing temperature, i.e., from 0.04 to 0.11.

It is also worth noting that no Ni-C or Fe-C bands were identified in the samples (Figure S2), thus, suggesting the absence of any C-doping.

Notwithstanding all these features, the existence of both metallic Ni^0 and Fe^0 is consistent with that observed in the XRD and SAED analyses as a result of the reduction process. In this respect, it is known that the XPS signal provides chemical information only from a thin layer with a few nanometers of thickness from the surface of nanoparticles. On the contrary, the XRD technique provides averaged information arising from many crystallites, where our samples show crystallite sizes ranging from 37 to 60 nm (see Figure 3). This discussion of both surface and bulk properties is, thus, crucial to provide insights into the performance of the produced electrocatalysts.

3.3. Mössbauer Spectroscopy and Magnetic Properties

The Mössbauer spectra of NiFe-500 and NiFe-700 samples are shown in Figures 7 and 8, respectively. Both spectra show the characteristics of slow relaxing magnetic moments; thus, the intensities of peaks do not have the relationship 3:2:1:1:2:3. For the sample NiFe-500, the spectrum is fit to three components (Figure 7). The first and second components are ascribed to Fe in NiFe-FCC and NiFe-BCC alloys; these components are fitted using a distribution of hyperfine magnetic fields (Hhf). The third component is a singlet that is related to a paramagnetic (PM) phase. There is no evidence of a Fe-Ni oxide phase. It is well known that Ni-ferrites have Hhf ranging from 51 to 54 T, and Figures 7 and 8 do not show features that could be ascribed to a Ni-ferrite phase. Figure 7a shows the experimental data and the fitting to the three components, while Figure 7b,c show the distributions of Hhf for Fe in NiFe-BCC and in NiFe-FCC solid solutions, respectively. Solid solution samples usually have some disorder and present a range of different nearest neighbors, and their Hhf will change depending on the amount of Fe nearest neighbors. The fit using a distribution of magnetic field indicates a central Fe atom with a different nearest neighbor. In BCC or FCC Fe-Ni structures, Fe atoms will have N = 8 or 12 nearest neighbors, respectively. Some of these neighbors may be Fe atoms. Thus, at any atomic position in the FCC structure of Fe_xNi_{1-x} alloys, the probability *P(n)* to obtain n Fe atoms in the first Fe coordination shell (and $N-n$, Ni atoms in the same first Fe coordination shell) is given in the following binomial distribution:

$$P(n) = \binom{N}{n} x^n (1-x)^{N-n} \quad (3)$$

where $n = 0, 1, 2, \ldots, N$. For a disordered FCC $Ni_{34}Fe_{66}$ alloy, the Fe coordination, which has high probabilities, is $P(4, 5, 6, 7, 8, 9, 10, 11) = (1.7, 5.2, 11.8, 19.6, 23.8, 20.5, 12.0, 4.2)\%$; these results evidence the need to use a distribution of Hhf to fit the spectrum of the disordered NiFe alloy. Table 2 shows the hyperfine parameters obtained from the fittings. The small isomer shift (IS) of the NiFe alloy is similar to the IS of α-Fe and reveals the metallic character of the Ni-Fe alloy. The Hhf of the Ni-Fe alloys was in the range of 26.5–27.5 T and 33.5 T for Fe in the FCC and BCC cells, respectively. The obtained Hhf and IS are in close agreement with earlier results presented by several authors [66–68]. These components show a very small quadrupole splitting (~0.002 mm/s), indicating a cubic lattice with a very small distortion due to Ni-Fe occupancies; this value is similar to the reported by Ping et al. [67] for metallic samples of Ni-Fe alloys.

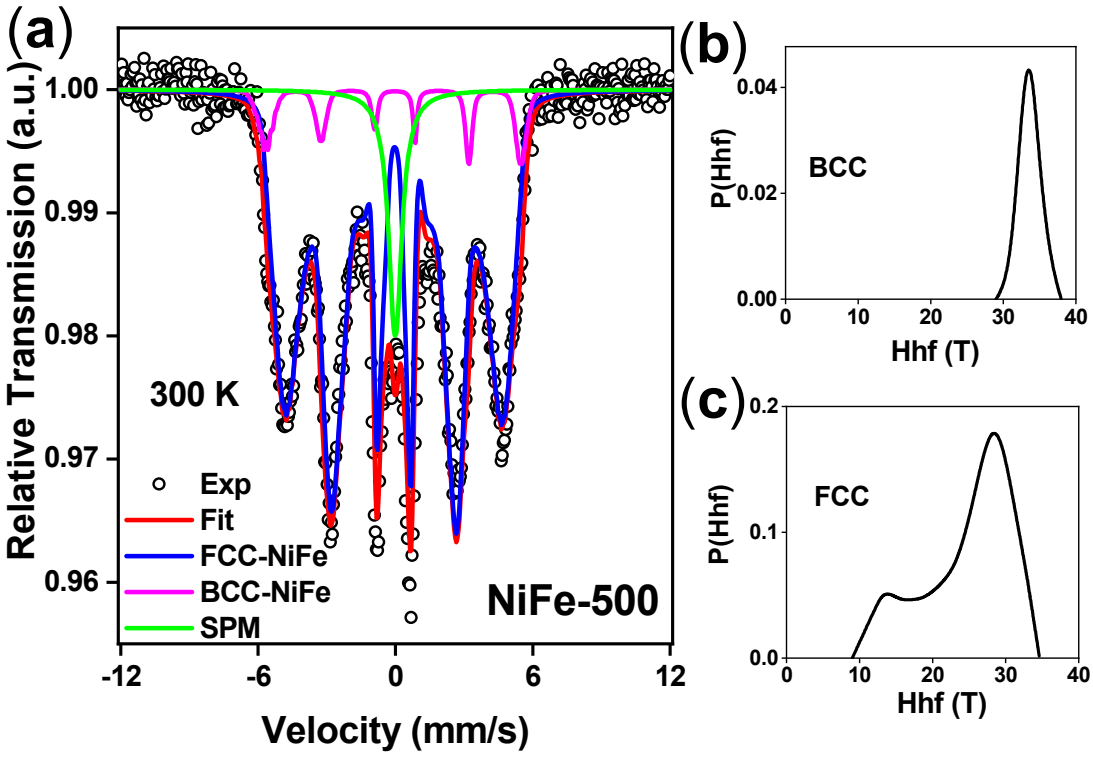

Figure 7. (**a**) Mössbauer spectrum recorded at 300 K for sample NiFe-500. (**b**) Distribution of magnetic fields for Fe in NiFe-BCC. (**c**) Distribution of magnetic fields for Fe in NiFe-FCC.

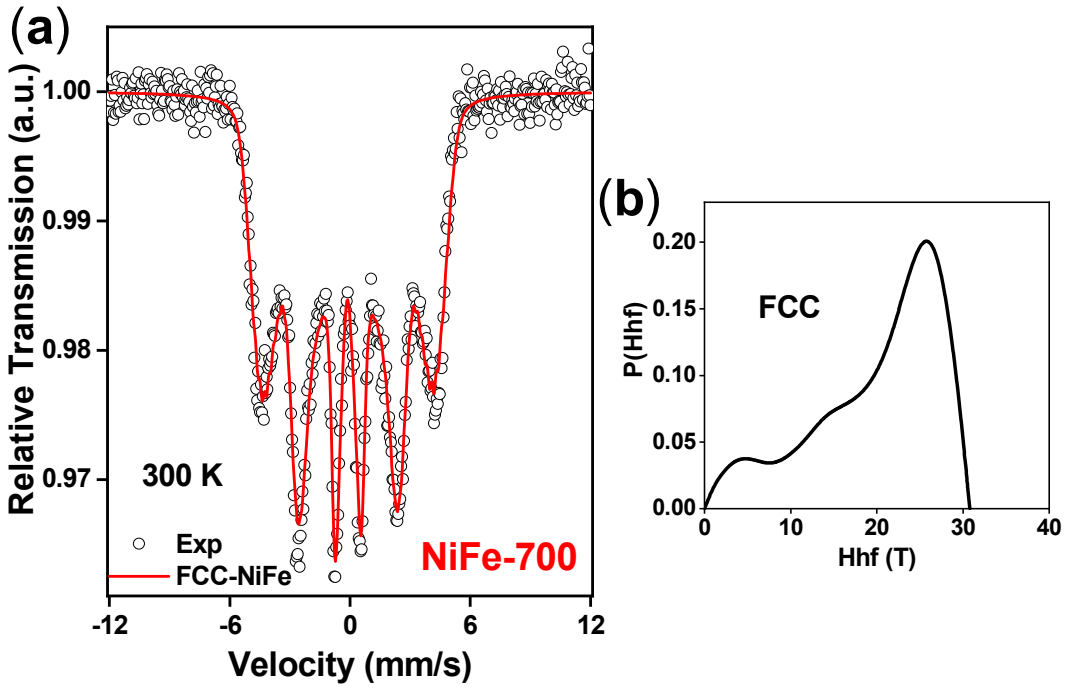

Figure 8. (**a**) Mössbauer spectrum recorded at 300 K for sample NiFe-700. (**b**) Distribution of magnetic field for Fe in NiFe-FCC.

The PM component may be attributed to the Fe-rich FCC Ni-Fe phase. It is well known that Fe-FCC (γ-Fe) is paramagnetic at 300 K. γ-Fe is known to show Curie–Weiss behavior with large negative Curie–Weiss temperature [69]. Early experimental studies have shown that this substance is a weak itinerant antiferromagnet with a Neel temperature of around

100 K [70]. A similar singlet component was found by Rodríguez et al. in a sample of $Fe_{67.5}Ni_{32.5}$ prepared by mechanical alloying. The authors assumed that this spectrum was due to γ-Fe-like clusters [71].

Table 2. Hyperfine parameters of spectra at 300 K for NiFe–500 and NiFe–700 samples.

Sample	Site	IS (mm/s)	Hhf (T)	Qs (mm/s)	RAA (%)
NiFe–500	Fe in FCC	0.042	27.5	−0.005	85
	Fe in BCC	0.068	33.5	−0.022	7
	Fe in PM	<0.035>	-	-	8
NiFe–700	Fe in FCC	0.021	26.5	-	100

For sample NiFe-700, the spectrum shown in Figure 8a is analyzed, accounting for an FCC phase. There is no presence of a paramagnetic or oxide phase, indicating that the reduction at 700 °C (NiFe-700) under H_2 is efficient in removing oxygen and transforming Ni and Fe cations into zerovalent metals. The spectrum was deconvoluted using a distribution of Hhf, as shown in Figure 8b, presenting a peak at 26.5 T and revealing the formation of the $Ni_{34}Fe_{66}$ FCC phase. This result is in close agreement with earlier reports [66,67] and is also in good accordance with the results obtained for the sample NiFe-500.

Magnetization measurements were performed at high temperatures to determine the temperatures at which the ferromagnetic phases become paramagnetic. For both samples, the magnetizations as a function of temperature in the range of 300–900 K are shown in Figures 9 and 10. The measurement for the sample NiFe-500 (Figure 9a) shows a peak at 455 K, and then the signal decreases following three distinct features. The peak at 455 K may be regarded as a blocking temperature of big particles. The other signals are better presented in Figure 9b, which shows the derivative of the magnetization, with peaks located at 533, 700, and 834 K. The first peak, at 533 K, represents the ferromagnetic Curie–Weiss transition for the phase $Ni_{37}Fe_{63}$-FCC, while the other peaks may be related to the phases $Ni_{46}Fe_{54}$-FCC and $Ni_{55}Fe_{45}$-FCC [72], respectively. The last two phases did not appear in the diffractogram, indicating they may be ascribed to very small crystallites that are below the detection limit of the XRD technique. The disordered BCC Ni-Fe alloy does not show a Curie–Weiss transition in the measured temperature range. In this regard, the magnetic transition for BCC Ni-Fe alloys is normally in the temperature range of 1020–1041 K; these values are beyond the temperatures accessible in our magnetometer setup (900 K) [72]. Figure 9c shows the plot of the inverse of magnetization versus temperature. The curve at temperatures above 834 K shows a clear downturn of magnetization and, therefore, does not show the linear behavior expected for a paramagnetic behavior following the Curie–Weiss law: $1/M = (T - \theta)/(CH)$, where C and θ are the Curie constant and the temperature Curie–Weiss, and H is the field used to run the measurement. The shoulder (downturn) close to 855 K seems, instead, to be indicative of the presence of the Griffiths phase that is due to short-range ordered ferromagnetic clusters embedded in a paramagnetic matrix. These clusters may be related to Fe clusters or to Ni-Fe alloys with poor Ni concentrations. Similar behavior of the (1/M) versus T curve has been observed in Y-Fe alloys [73], in the ferromagnetic solid solutions $Ni(1 - x)V(x)$ [74] and $Ni(1 - x)Cu(x)$ [75]. In fact, in the alloy $Ni(1 - x)V(x)$, the ferromagnetic transition can be tuned by substituting V for Ni in the paramagnetic phase, and large magnetic clusters with giant local moments were observed. The shoulder in the (1/M) versus T curve is ascribed to the Griffiths phase, and it is usually studied through the relationship:

$$1/M \sim (T - Tcm)^{1-\lambda} \quad (4)$$

where λ is the susceptibility exponent and should be smaller than unity, and Tcm and λ are the fitting parameters [73]. The presence of the Griffiths phase is in agreement with a disordered Ni-Fe alloy, as evidenced in the Mössbauer study.

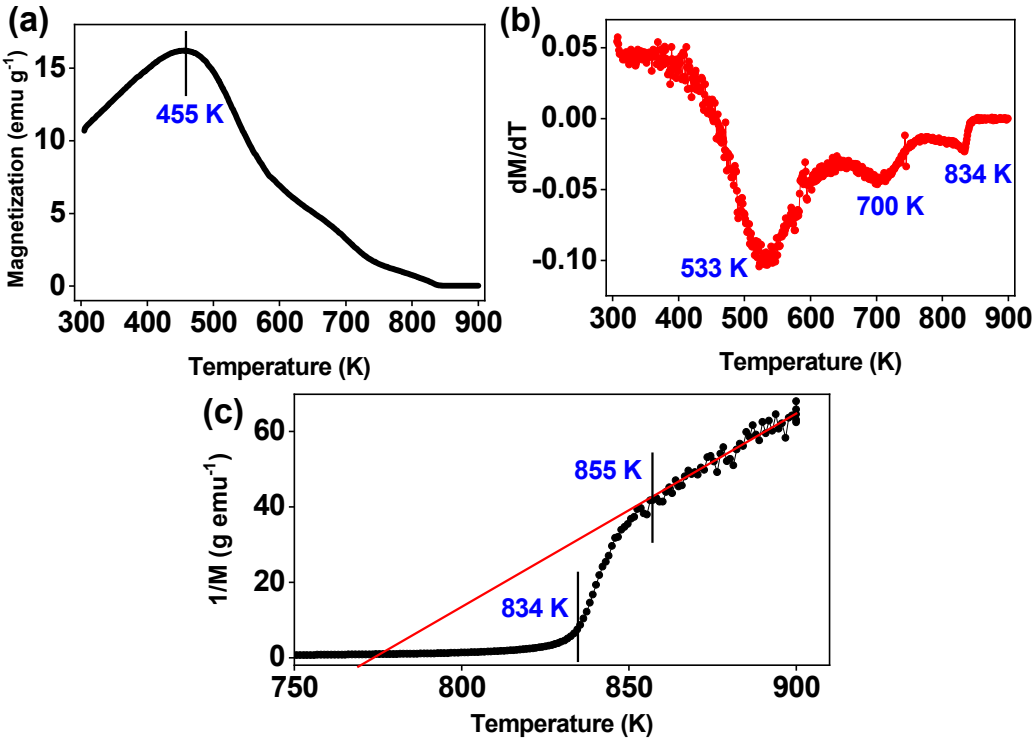

Figure 9. (**a**) Magnetization versus temperature (range of 300–900 K) measured at H = 160 Oe of sample NiFe-500. (**b**) Derivative of the M-T measurement. (**c**) Inverse to magnetization versus temperature, the red line is the fit of the 855–900 K range data.

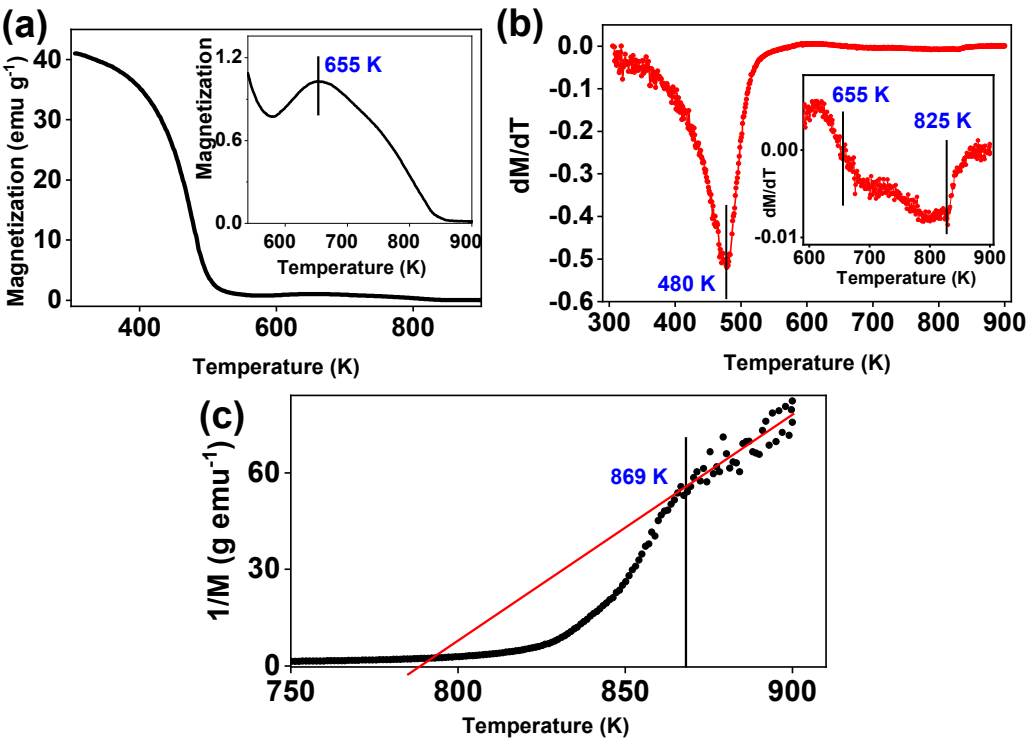

Figure 10. (**a**) Magnetization versus temperature (range of 300–900 K) measured under H = 160 Oe and enlarged view in the range of 540–900 K of sample NiFe-700. (**b**) Derivative of the M-T measurement and enlarged view in the range of 590–900 K. (**c**) Inverse of magnetization versus temperature, the red line is the fit of the 869–900 K range data.

Magnetization as a function of temperature for sample NiFe-700 is shown in Figure 10a. In the temperature range of 300–550 K, it presents a monotonous behavior, decreasing smoothly with increasing temperature until 550 K. However, at temperatures above 550 K (see insert in Figure 10a), a fast upward signal is observed, peaking at 655 K. Beyond this temperature, the signal decreases, reaching a very small value at temperatures above 850 K. The derivative of the M-T measurement is shown in Figure 10b, clearly demonstrating several magnetic transitions. The peak at 480 K is very intense, indicating a large contribution of the FCC $Ni_{34}Fe_{66}$ alloy [72]. Furthermore, in the range between 600 and 850 K, there are several peaks with small intensities, indicating Fe-rich $Ni_{1-x}Fe_x$ alloys with ferromagnetic transitions approximately in the range of 655 K (FCC $Ni_{43}Fe_{57}$) to 825 K (FCC $Ni_{54}Fe_{46}$) [72]. Figure 10c shows the curve (1/M) versus T, revealing it to have similar behavior as seen in the sample NiFe-500 in Figure 9c; the downturn of magnetization occurs at a temperature of 869 K. This indicates that the sample NiFe-700 also has the presence of Fe clusters embedded in the paramagnetic matrix due to the Ni-Fe alloys.

Figure 11 shows the M versus H measurements at 5 K, while Table 3 gathers all the magnetic parameters collected from the M-H measurements (Ms, Mr, Mr/Ms, and Hc). The saturation magnetization (Ms) can be determined from the law of approach to saturation, $M(H) = Ms(1 + b/H^2)$, where b is a fitting constant related to the magnetocrystalline anisotropy of the alloy, and the M(H) data are chosen such as H >> Hc (Hc is the coercivity field) [76]. Since each sample has alloys with several concentrations of Ni and Fe, it is difficult to assign the magnetocrystalline anisotropy constant that one can calculate from the fitting parameter, b. The fittings of the M versus H^{-2} curves for magnetic fields above 80 kOe are shown in Figure 12a,b.

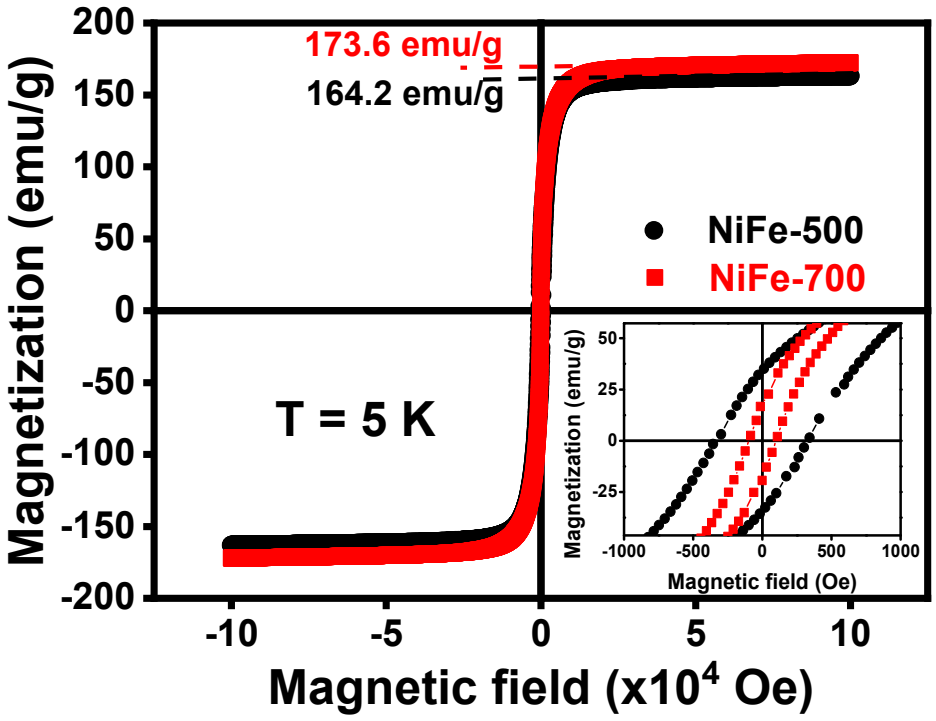

Figure 11. Magnetic hysteresis measured at 5 K for samples obtained from reduction of $NiFe_2O_4$ at 500 °C (NiFe-500) and 700 °C (NiFe-700). Insert shows an enlarged view of data around H = 0.

Table 3. Magnetic parameters from the M-H measurements recorded at 5 K.

Sample	Ms (emu/g)	Mr (emu/g)	Mr/Ms	Hc (Oe)
NiFe-500	164.2	34.27	0.21	335.45
NiFe-700	173.6	17.58	0.10	98.83

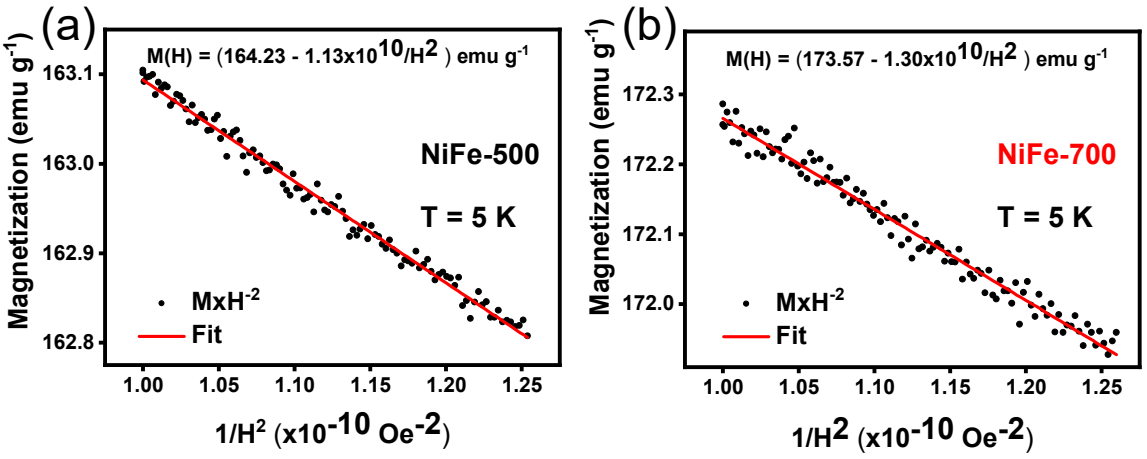

Figure 12. Linear fittings of the magnetization versus $1/H^2$ curves recorded at 5 K for samples (**a**) NiFe-500 and (**b**) NiFe-700. The equation in each figure is regarded as the linear fitting.

The saturation magnetization (Ms) for samples NiFe-500 and NiFe-700 are 164.2 emu g^{-1} and 173.6 emu g^{-1}, respectively. These values are larger than the Ms expected for the phases found in the XRD and M-T analysis. According to the literature [76], for FCC $Fe_{1-x}Ni_x$ alloys, the largest Ms value of ~158 emu g^{-1} corresponds to FCC $Fe_{0.54}Ni_{0.46}$. In this present work, for both samples, the presence of alloys with molar ratios $x/(1-x)$ larger than 1/2 was found, indicating the formation of alloys with a Ni concentration above 33%. Since the nominal amount of Ni used to prepare the samples was 33%, it is clear that besides the alloys found in both samples, there should be alloys with a very large Fe concentration and also pure Fe clusters. The presence of the Griffiths phase at temperatures above 855 and 869 K is strong evidence that the Fe clusters and BCC-NiFe alloys enhance the saturation magnetizations in both samples. In the lower-right insert, there is an enlarged view of the low magnetic field region, showing the remanence magnetization (Mr) and the coercivity field (Hc) for these samples. Their coercivity fields indicate the soft magnetic character of these samples. However, since the XPS study has indicated that there is a thin oxide shell at the surface of nanoparticles, the magnetic moments at the surface may be disordered and pinned, thus, enhancing the Hc.

3.4. Electrochemistry Characterization

The electrocatalytic activities of the Ni-Fe alloy nanoparticles as anodes for OER were evaluated in an alkaline medium (1 M KOH), where polarization curves are obtained via linear sweep voltammetry. Figure 13a shows the activity of the NiFe-500, NiFe-700, and blank Ni foam electrodes (used as a reference). From the results, it follows that to generate a current density of j = 10 mA cm^{-2}, the overpotential reached by blank Ni foam was 517 mV, which is much higher than the 319 mV required for NiFe-500 and 307 mV for NiFe-700. In addition to the good performance at the reference current (J = 10 mA cm^{-2}), the NiFe-700 electrode can achieve high current densities (400 mA cm^{-2} at 490 mV) below 500 mV, which is a desirable characteristic for commercial electrodes [77]. In this respect, the NiFe-500 should exhibit a smaller overpotential at 10 mA cm^{-2} due to its smaller-sized nanoparticles (see Figures 4 and 5). Nonetheless, the best performance for OER is given by the sample NiFe-700. This result can be explained by the undesirable presence of the BCC crystal structure in NiFe-500. The BCC phase has lower catalytic activity than the FCC phase due to the small number of atoms exposed on each face (see crystal structures in Figure 3). Among all the possible structures for Ni-Fe alloy crystallization, the number of atoms exposed is greater in the HCP structure, followed by FCC and BCC [37].

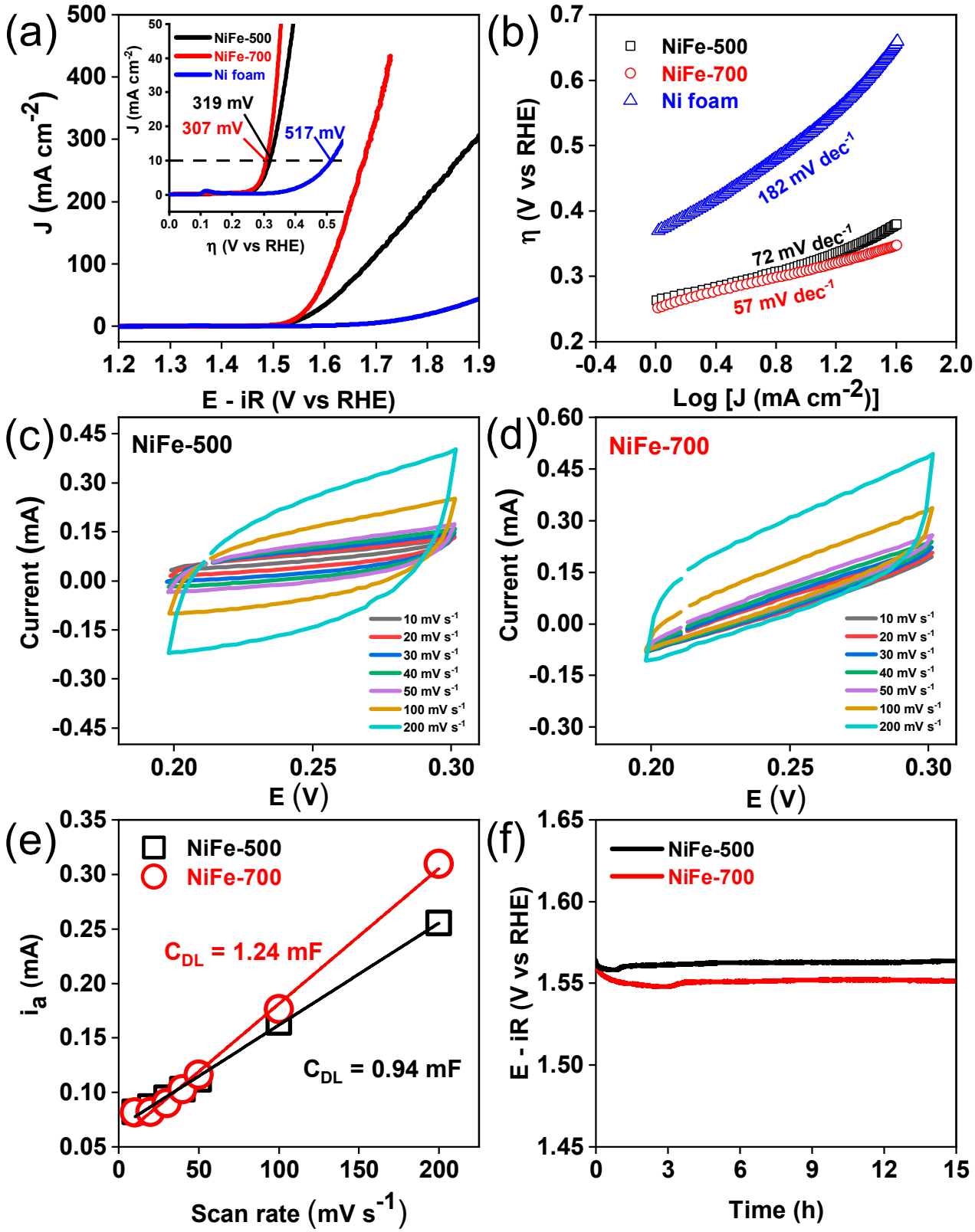

Figure 13. (**a**) LSV and (**b**) Tafel slope for NiFe-500, NiFe-700, and blank Ni foam electrodes; cyclic voltammetry of 10–200 mV s^{-1} for (**c**) NiFe-500 (**c**,**d**) NiFe-700; (**e**) plot of anodic current (i_a) versus scan rate to determine C_{DL}; (**f**) chronopotentiometry at J = 10 mA cm^{-2} for a period of 15 h (**f**).

The NiFe-500 overpotential is compatible with that of Fe, Ni-based materials prepared via the solution blow spinning (NiFe-$NiFe_2O_4$, η = 316 mV) [25] and electrodeposition in DES ($Ni_{75}Fe_{25}$ (η = 316 mV) and $Ni_{50}Fe_{50}$ (η = 321 mV)) [40], while the NiFe-700 is similar to the Ni-Fe-P alloy (η = 309 mV) [78] and NiFe hydroxide (η = 310 mV) [79] prepared using the methodologies of direct-current electrodeposition and mild two-step hydrothermal reaction, respectively.

Tafel slope was used to provide information about surface kinetics and to help elucidate the reaction mechanism on the OER [80]. The slopes can be obtained from the Tafel equation as follows (Equation (5)):

$$\eta = a + b \log (j_0) \quad (5)$$

where η is the overpotential, a is the intercept relative to the exchange current density j_0, and b is the Tafel slope [81]. As shown in Figure 13b, the values of the Tafel slopes were 57, 72 e 182 mV dec^{-1} for NiFe-700, NiFe-500, and blank Ni foam, respectively. The lowest value found for the NiFe-700 sample implies faster kinetics for OER, which can be attributed to a greater number of active sites. In addition, a Tafel value found close to 60 mV dec^{-1} for the Ni-Fe-based electrodes suggests that the adsorption of intermediate species is the rate-determining step, in accordance with Krasil'shchikov's reaction model for the four-step OER in alkaline solution as follows (Equations (6)–(9), where M is the active metal) [25,82]:

$$M + OH^- \rightarrow M - OH + e^-, \qquad b = 120 \text{ mV } dec^{-1} \quad (6)$$

$$M - OH + OH^- \rightarrow M - O^- + H_2O, \qquad b = 60 \text{ mV } dec^{-0} \quad (7)$$

$$M - O^- \rightarrow M - O + e^-, \qquad b = 45 \text{ mV } dec^{-5} \quad (8)$$

$$2M - O \rightarrow 2M + O_2, \qquad b = 19 \text{ mV } dec^{-9} \quad (9)$$

The area of the electrode that is effectively exposed to the electrolyte, which is the electrochemically active surface area (ECSA), was estimated using cyclic voltammetry (CV) to obtain the double layer capacitance (C_{DL}). Figure 13c,d shows the results of the CV curves obtained for the NiFe-500 and NiFe-700 electrodes performed in a non-Faradaic region (1.2–1.3 V vs. RHE) with a scan rate of 10 to 200 mV s^{-1}. Then, C_{DL} values were extracted from the relation anodic current (i_a) measured at 1.25 V vs. RHE versus scan rate (v), according to ($i_a = v \times C_{DL}$) [83].

Figure 13e shows that the NiFe-700 electrode has a C_{DL} value = 1.24 mF, against 0.94 mF for NiFe-500, which refers to a much larger ECSA for the NiFe-700 electrode given the relation ($ECSA = C_{DL}/C_S$), where C_S is the specific capacitance and for electrodes based on Ni-Fe in alkaline solution is equivalent to 0.040 mF cm^{-2} [25,81,83]. Thus, the calculated ECSA values were 31 cm^2 (NiFe-700) and 23.5 cm^2 (NiFe-500), which are in accordance with electrodes based on Ni-Fe alloys [81]. Therefore, the higher ECSA value presented by the NiFe-700 electrode is a clear reason for its better electrochemical performance.

The operational stability test was performed using chronopotentiometry in an alkaline solution (1 M KOH) for an uninterrupted period of 15 h and a constant current density of J = 10 mA cm^{-2} (see Figure 13f). Both electrodes showed a small increase negligible in overpotential of ≈13 mV vs. RHE to maintain the applied current density. This has been attributed to the blocking of the active sites by the generated O_2 bubbles [25]. Table 4 summarizes some NiFe-based electrocatalysts reported in the literature.

Table 4. Comparison of the performance of several NiFe-based electrocatalysts for OER reported in the literature.

Catalyst	Substrate	Synthesis Method	η_{10} (mV vs. RHE)/ Electrolyte	Tafel Slope (mV dec^{-1})	Reference
NiFe-500 NPs	Ni foam	Sol–gel synthesis followed by a reduction in H_2	319	72	This work
NiFe-700 NPs			307	57	
NiFe-$NiFe_2O_4$ fibers	Ni foam	Solution blow spinning	316	74	[25]
NiFe foam	NiFe foam	-	320	56	[41]
NiFe thin films	Platinum mesh	Thermal evaporation	370	37	[42]
NiFe/graphene	PT foil	Hummers' method followed by electrodeposition	350	59	[84]
NiFe/CC	carbon cloth	Chemical bath at room temperature followed by reduction	281–340	64–71	[81]
NiFe LDH	glassy carbon	Hydrothermal process	347	67	[85]
NiFeO	GC	Coprecipitation	328	42	[86]
NiFe/Au	Au-RDE	Electrodeposition	330	58	[87]
$Ni_{0.9}Fe_{0.1}$/NC	GC	Pyrolysis	330	45	[88]
NiFeOH/NF	NF	Impregnation	342	55	[89]
Ni-Fe-P Alloy	GC	Direct-current electrodeposition	309	79.4	[78]
Ni NP/NiFe LDH	-	Hydrothermal method	328	62	[90]
NiFe LDH	GC	Hydrothermal method	328	59.9	[91]
FeNi-FeNiO/CNS-700	GC	Phosphating process	355	80.1	[92]
NiFe-LDH/NF	Ni foam	Electrodeposition	370	131.2	[93]
NiFe hydroxide	GC	Mild two-step hydrothermal reaction	310	107	[79]
$Ni_{4/5}Fe_{1/5}$-LDHs	GC	Hydrothermal method	325	86.1	[94]
$Ni_{75}Fe_{25}$	Cu foil	Electrodeposition in DES	316	62	[40]
$Ni_{50}Fe_{50}$			321	58	
$Ni_{25}Fe_{75}$			361	44	

The kinetic study of the electrocatalysts was conducted using electrochemical impedance spectroscopy (EIS) in the OER regime (at a DC potential of 1.6 V vs. RHE by 15 min for stabilization) for NiFe-500 and NiFe-700 electrodes. As shown in Figure 14a, the Nyquist plots reveal the presence of a single semicircle, describing the electrode impedance, confirmed by the Bode plots in Figure 14b. Thus, a Randles circuit ($R_S(R_{CT}CPE)$), inserted in Figure 14a, considering the whole process governed by a one-time constant ($\tau = RC$), was adopted in this study. In this circuit, Rs and R_{CT} represent the solution and charge transfer resistance, respectively, and CPE is a constant phase element. The double layer capacitance (C_{DL}) was calculated from CPE parameters according to the expression: $C_{DL} = R_{CT}^{(1-n)/n}CPE^{1/n}$ [80]. NiFe-700 electrode showed a lower RS value, suggesting a good electrical contact between the catalyst and substrate [95]. In addition, the low solution impedance favors current flow through the electrolyte by the mobility of ions. Since RCT is related to the overall OER rate [96], the low impedance of the NiFe-700 electrode confirms its better performance towards OER. The CDL values for both electrodes were expected to be higher than those obtained using CV (Figure 13e) due to Faradic contributions in the OER regime and adsorption (intermediate species). All fitting results are listed in Table 5.

Table 5. EIS—Fitting results of the impedance spectra in Figure 14.

Electrode	R_S (Ω)	R_{CT} (Ω)	CPE ($S.s^{-1}$)	n	C_{DL} (mF)
NiFe-500	2.48 ± 0.004	1.22 ± 0.006	0.00339 ± 0.0001	0.8689 ± 0.0050	1.49
NiFe-700	1.75 ± 0.003	1.16 ± 0.004	0.00407 ± 0.0001	0.8569 ± 0.0047	1.67

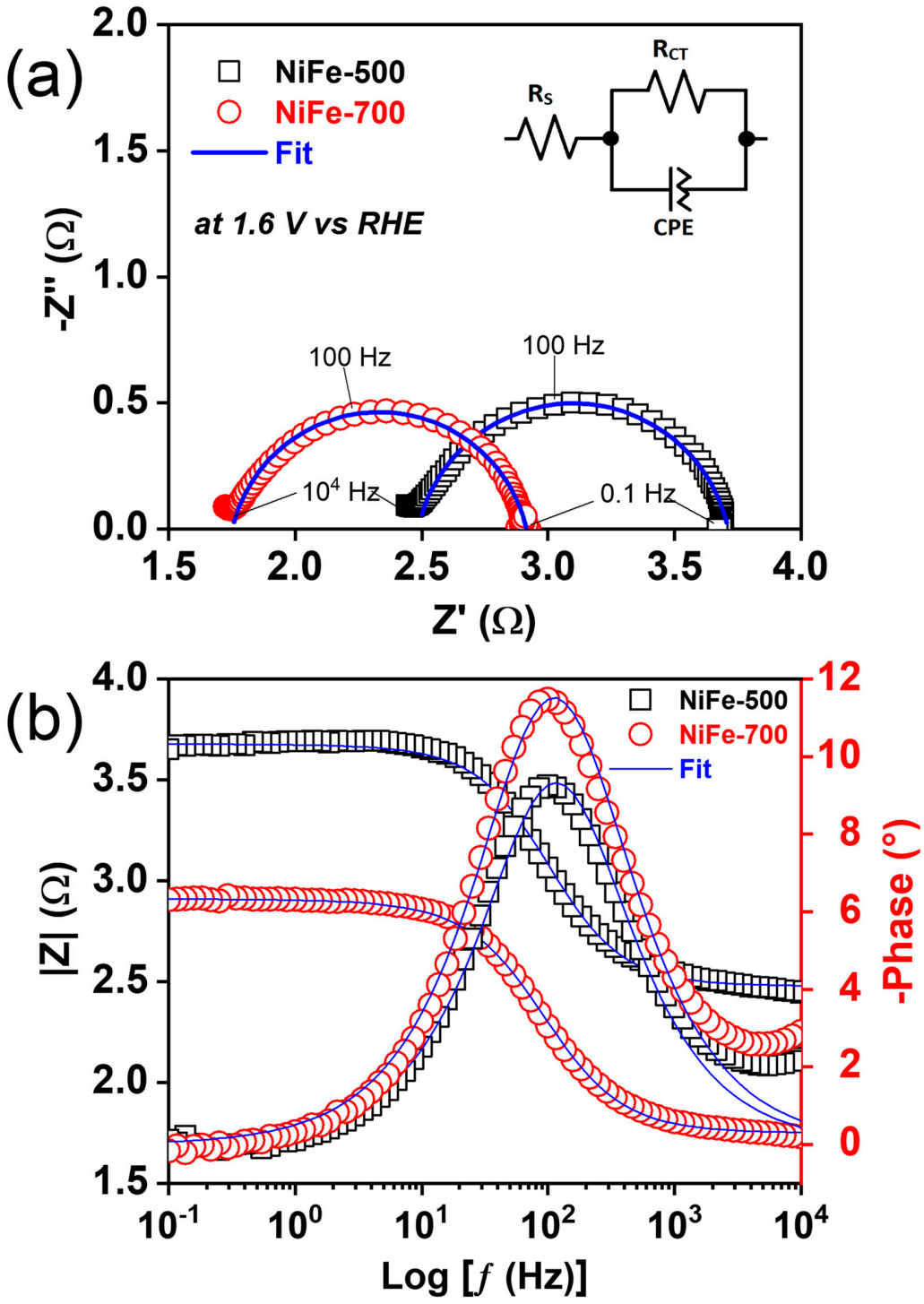

Figure 14. (**a**) Nyquist and (**b**) Bode plots obtained at DC potential of 1.6 V vs. RHE for NiFe-500 and NiFe-700, respectively, inserted in (**a**) the Randles circuit model, ($R_S(R_{CT}CPE)$), and used to fit the spectra.

4. Conclusions

Ni-Fe alloy Nps were successfully prepared using the proteic sol–gel method and chemical reduction in H_2. The Ni-Fe alloy nanoparticles had crystallite sizes in the range of 37 to 60 nm. The samples showed the presence of alloy phases with several compositions leading to several FM transitions. A very thin layer of surface oxides was also formed as shown by XPS. However, XRD and Mössbauer spectroscopy studies showed only metal phases. M vs. T measurements at high temperatures evidences the presence of the Griffiths

phase due to clusters rich in Fe. The M vs. H measurements, at 5 K, showed Ms values of 164.2 and 173.6 emu g^{-1} for the samples NiFe-500 and NiFe-700, respectively. These results indicated the higher content of the Ni-Fe alloy phases. Finally, the electrocatalysts showed promising low overpotentials of 319 and 307 mV at 10 mA cm^{-2} and high electrochemical stability.

Supplementary Materials: The following supporting information can be downloaded at: https://www.mdpi.com/article/10.3390/magnetochemistry9080201/s1. Figure S1: Overview XPS spectra of (a) NiFe-500 and (b) NiFe-700 samples, Figure S2: High-resolution XPS spectra of the C 1s bands in (a) NiFe-500 and (b) NiFe-700 samples.

Author Contributions: Conceptualization, R.A.R., D.A.M. and M.A.M.; methodology, R.A.R., V.D.S., L.S.F., F.J.A.L. and D.P.F.; validation, R.A.R., V.D.S., L.S.F. and F.J.A.L.; formal analysis, R.A.R., V.D.S., L.S.F. and F.J.A.L.; investigation, R.A.R., D.A.M. and M.A.M.; resources, D.A.M., U.U.G., M.M.S., R.M.G. and D.P.F.; data curation, D.A.M., U.U.G. and M.M.S.; writing—original draft preparation, V.D.S., D.A.M., F.J.A.L., R.A.R. and M.A.M.; writing—review and editing, R.A.R., D.A.M. and M.A.M.; supervision, R.M.G., D.A.M. and M.A.M. All authors have read and agreed to the published version of the manuscript.

Funding: This research was funded by PTDC/CTM-CTM/2156/2020, PTDC/QUI-ELT/3681/2020, POCI-01-0247-FEDER-039926, POCI-01-0145-FEDER-032241, UIDB/00481/2020, UIDP/00481/2020, and CENTRO-01-0145-FEDER-022083—Centro Portugal Regional Operational Programe (Centro2020) under the PORTUGAL 2020 Partnership Agreement through the European Regional Development Fund (ERDF).

Institutional Review Board Statement: Not applicable.

Informed Consent Statement: Not applicable.

Data Availability Statement: Data are contained within the article or Supplementary Material.

Acknowledgments: Rafael A. Raimundo, Luciena S. Ferreira, and Vinícius D. Silva thank the CAPES, Finance Code 001. Daniel A. Macedo and Marco A. Morales acknowledge the Brazilian National Research Council—CNPq, 309430/2019-4 and 313337/2018-7. Duncan P. Fagg and Francisco J. A. Loureiro acknowledge the projects PTDC/CTM-CTM/2156/2020, PTDC/QUI-ELT/3681/2020, POCI-01-0247-FEDER-039926, POCI-01-0145-FEDER-032241, UIDB/00481/2020, UIDP/00481/2020, and CENTRO-01-0145-FEDER-022083—Centro Portugal Regional Operational Programme (Centro2020) under the PORTUGAL 2020 Partnership Agreement through the European Regional Development Fund (ERDF). We thank Igor Zumba Damasceno and Carla Laize dos Santos Cruz Costa of LCEM-UFRN for providing the FESEM images and Tatiane Oliveira dos Santos at LABMIC-UFG for providing the TEM images.

Conflicts of Interest: The authors declare no conflict of interest.

References

1. Li, H.; Liaw, P.K.; Choo, H.; Tabachnikova, E.D.; Podolskiy, A.V.; Smirnov, S.N.; Bengus, V.Z. Temperature-dependent mechanical behavior of a nanostructured Ni–Fe alloy. *Mater. Sci. Eng. A* **2008**, *493*, 93–96. [CrossRef]
2. Gheisari, K.; Javadpour, S.; Oh, J.; Ghaffari, M. The effect of milling speed on the structural properties of mechanically alloyed Fe–45%Ni powders. *J. Alloys Compd.* **2009**, *472*, 416–420. [CrossRef]
3. Liu, Y.; Qin, M.; Zhang, L.; Huang, M.; Li, S.; Jia, B.; Zhang, D.; Qu, X. Solution combustion synthesis of nanocrystalline Fe–50%Ni alloy powder. *Powder Technol.* **2014**, *267*, 68–73. [CrossRef]
4. Nirouei, M.; Jafari, A.; Boustani, K. Magnetic and Structural Study of $FeNi_3$ Nanoparticles: Effect of Calcination Temperature. *J. Supercond. Nov. Magn.* **2014**, *27*, 2803–2811. [CrossRef]
5. Margeat, O.; Ciuculescu, D.; Lecante, P.; Respaud, M.; Amiens, C.; Chaudret, B. NiFe Nanoparticles: A Soft Magnetic Material? *Small* **2007**, *3*, 451–458. [CrossRef] [PubMed]
6. Veiseh, O.; Gunn, J.W.; Zhang, M. Design and fabrication of magnetic nanoparticles for targeted drug delivery and imaging. *Adv. Drug Deliv. Rev.* **2010**, *62*, 284–304. [CrossRef] [PubMed]
7. Khramtsov, P.; Kropaneva, M.; Byzov, I.; Minin, A.; Mysik, A.; Timganova, V.; Bochkova, M.; Uimin, M.; Zamorina, S.; Yermakov, A.; et al. Conjugation of carbon coated-iron nanoparticles with biomolecules for NMR-based assay. *Colloids Surf. B Biointerfaces* **2019**, *176*, 256–264. [CrossRef] [PubMed]

8. Azizi, A.; Sadrnezhaad, S. Synthesis of Fe–Ni nano-particles by low-temperature hydrogen reduction of mechanically alloyed Ni-ferrite. *J. Alloys Compd.* **2009**, *485*, 484–487. [CrossRef]
9. Abellán, G.; Coronado, E.; Martí-Gastaldo, C.; Ribera, A.; Otero, T.F. Magnetic Nanocomposites Formed by $FeNi_3$ Nanoparticles Embedded in Graphene. Application as Supercapacitors. *Part. Part. Syst. Charact.* **2013**, *30*, 853–863. [CrossRef]
10. Feng, Y.; Qiu, T. Enhancement of electromagnetic and microwave absorbing properties of gas atomized Fe-50wt%Ni alloy by shape modification. *J. Magn. Magn. Mater.* **2012**, *324*, 2528–2533. [CrossRef]
11. Arnold, H.D.; Elmen, G.W. Permalloy, A New Magnetic Material of Very High Permeability. *Bell Syst. Tech. J.* **1923**, *2*, 101–111. [CrossRef]
12. Tabakovic, I.; Inturi, V.; Thurn, J.; Kief, M. Properties of $Ni_{1-x}Fe_x$ ($0.1 < x < 0.9$) and Invar ($x = 0.64$) alloys obtained by electrodeposition. *Electrochim. Acta* **2010**, *55*, 6749–6754. [CrossRef]
13. Mccrea, J.L.; Palumbo, G.; Hibbard, G.D.; Erb, U. Properties and applications for electrodeposited nanocrystalline Fe-Ni alloys. *Rev. Adv. Mater. Sci.* **2003**, *5*, 252–258.
14. Heck, D.C. *Magnetic Materials and Their Applications*; Elsevier: Amsterdam, The Netherlands, 1974; Volume 392.
15. Liu, Y.; Chi, Y.; Shan, S.; Yin, J.; Luo, J.; Zhong, C.-J. Characterization of magnetic NiFe nanoparticles with controlled bimetallic composition. *J. Alloys Compd.* **2014**, *587*, 260–266. [CrossRef]
16. Dijith, K.S.; Aiswarya, R.; Praveen, M.; Pillai, S.; Surendran, K.P. Polyol derived Ni and NiFe alloys for effective shielding of electromagnetic interference. *Mater. Chem. Front.* **2018**, *2*, 1829–1841. [CrossRef]
17. Yekta, P.V.; Sharifi, E.M.; Ghasemi, A. The effect of thermomechanical treatment on the magnetic and mechanical properties of Fe-48Ni alloy. *Phys. B Condens. Matter* **2019**, *558*, 28–37. [CrossRef]
18. Kurichenko, V.L.; Karpenkov, D.Y.; Karpenkov, A.Y.; Lyakhova, M.B.; Khovaylo, V.V. Synthesis of FeNi tetrataenite phase by means of chemical precipitation. *J. Magn. Magn. Mater.* **2019**, *470*, 33–37. [CrossRef]
19. Singh, N.; Parkash, O.; Kumar, D. Phase evolution, mechanical and corrosion behavior of $Fe_{(100-x)}$ $Ni_{(x)}$ alloys synthesized by powder metallurgy. *J. Phys. Chem. Solids* **2018**, *114*, 8–20. [CrossRef]
20. Bouremana, A.; Guittoum, A.; Hemmous, M.; Martínez-Blanco, D.; Gorria, P.; Blanco, J. Low temperature hydrothermal synthesis of $Ni_{75}Fe_{25}$ nanostructured powders: Microstructure, morphology and magnetic behaviour. *J. Magn. Magn. Mater.* **2018**, *466*, 212–218. [CrossRef]
21. Zhang, B.; Fenineche, N.-E.; Liao, H.; Coddet, C. Magnetic properties of in-situ synthesized $FeNi_3$ by selective laser melting Fe-80%Ni powders. *J. Magn. Magn. Mater.* **2013**, *336*, 49–54. [CrossRef]
22. Sun, X.; Zhang, X.; Wang, P.; Yang, M.; Ma, J.; Ding, Z.; Geng, B.; Wang, M.; Ma, Y. Evolution of structure and magnetism from $NixFe_{3-x}O_4$ ($x = 0$, 0.5, 1 and 1.5) to Ni-Fe alloys and to Ni-Fe-N. *Mater. Res. Bull.* **2017**, *95*, 261–266. [CrossRef]
23. Kanhe, N.S.; Kumar, A.; Yusuf, S.M.; Nawale, A.B.; Gaikwad, S.S.; Raut, S.A.; Bhoraskar, S.V.; Wu, S.Y.; Das, A.K.; Mathe, V.L. Investigation of structural and magnetic properties of thermal plasma-synthesized $Fe_{1-x}Ni_x$ alloy nanoparticles. *J. Alloys Compd.* **2016**, *663*, 30–40. [CrossRef]
24. Poroch-Seritan, M.; Cretescu, I.; Cojocaru, C.; Amariei, S.; Suciu, C. Experimental design for modelling and multi-response optimization of Fe–Ni electroplating process. *Chem. Eng. Res. Des.* **2015**, *96*, 138–149. [CrossRef]
25. Raimundo, R.A.; Silva, V.D.; Medeiros, E.S.; Macedo, D.A.; Simões, T.A.; Gomes, U.U.; Morales, M.A.; Gomes, R.M. Multifunctional solution blow spun NiFe–$NiFe_2O_4$ composite nanofibers: Structure, magnetic properties and OER activity. *J. Phys. Chem. Solids* **2020**, *139*, 109325. [CrossRef]
26. Xiang, J.; Shen, X.; Song, F.; Liu, M.; Zhou, G.; Chu, Y. Fabrication and characterization of Fe–Ni alloy/nickel ferrite composite nanofibers by electrospinning and partial reduction. *Mater. Res. Bull.* **2011**, *46*, 258–261. [CrossRef]
27. Leite, G.; Chagas, E.; Pereira, R.; Prado, R.; Terezo, A.; Alzamora, M.; Baggio-Saitovitch, E. Exchange coupling behavior in bimagnetic $CoFe_2O_4$/$CoFe_2$ nanocomposite. *J. Magn. Magn. Mater.* **2012**, *324*, 2711–2716. [CrossRef]
28. Yourdkhani, A.; Ebrahimi, S.S.; Koohdar, H. Preparation of strontium hexaferrite nano-crystalline powder by carbon monoxide heat treatment and re-calcination from conventionally synthesized powder. *J. Alloys Compd.* **2009**, *470*, 561–564. [CrossRef]
29. Koohdar, H.; Ebrahimi, S.S.; Yourdkhani, A.; Dehghan, R.; Zajkaniha, F. Optimization of hydrogen dynamic heat treatment and re-calcination for preparation of strontium hexaferrite nanocrystalline powder. *J. Alloys Compd.* **2009**, *479*, 638–641. [CrossRef]
30. Hessien, M.; Radwan, M.; Rashad, M. Enhancement of magnetic properties for the barium hexaferrite prepared through ceramic route. *J. Anal. Appl. Pyrolysis* **2007**, *78*, 282–287. [CrossRef]
31. Lima, E.; Drago, V.; Fichtner, P.F.; Domingues, P.H. Tetrataenite and other Fe–Ni equilibrium phases produced by reduction of nanocrystalline $NiFe_2O_4$. *Solid State Commun.* **2003**, *128*, 345–350. [CrossRef]
32. Azizi, A.; Yoozbashizadeh, H.; Sadrnezhaad, S. Effect of hydrogen reduction on microstructure and magnetic properties of mechanochemically synthesized Fe–16.5Ni–16.5Co nano-powder. *J. Magn. Magn. Mater.* **2009**, *321*, 2729–2732. [CrossRef]
33. Zhao, Q.; Yan, Z.; Chen, C.; Chen, J. Spinels: Controlled Preparation, Oxygen Reduction/Evolution Reaction Application, and Beyond. *Chem. Rev.* **2017**, *117*, 10121–10211. [CrossRef]
34. Mohammed-Ibrahim, J. A review on NiFe-based electrocatalysts for efficient alkaline oxygen evolution reaction. *J. Power Sources* **2020**, *448*, 227375. [CrossRef]
35. Fan, Z.; Zhang, H. Crystal phase-controlled synthesis, properties and applications of noble metal nanomaterials. *Chem. Soc. Rev.* **2016**, *45*, 63–82. [CrossRef] [PubMed]

36. Wu, Z.-P.; Shan, S.; Xie, Z.-H.; Kang, N.; Park, K.; Hopkins, E.; Yan, S.; Sharma, A.; Luo, J.; Wang, J.; et al. Revealing the Role of Phase Structures of Bimetallic Nanocatalysts in the Oxygen Reduction Reaction. *ACS Catal.* **2018**, *8*, 11302–11313. [CrossRef]
37. Wang, C.; Yang, H.; Zhang, Y.; Wang, Q. NiFe Alloy Nanoparticles with hcp Crystal Structure Stimulate Superior Oxygen Evolution Reaction Electrocatalytic Activity. *Angew. Chem.* **2019**, *131*, 6160–6164. [CrossRef]
38. Gu, J.; Guo, Y.; Jiang, Y.-Y.; Zhu, W.; Xu, Y.-S.; Zhao, Z.-Q.; Liu, J.-X.; Li, W.-X.; Jin, C.-H.; Yan, C.-H.; et al. Robust Phase Control through Hetero-Seeded Epitaxial Growth for Face-Centered Cubic Pt@Ru Nanotetrahedrons with Superior Hydrogen Electro-Oxidation Activity. *J. Phys. Chem. C* **2015**, *119*, 17697–17706. [CrossRef]
39. Kim, J.; Lee, Y.; Sun, S. Structurally Ordered FePt Nanoparticles and Their Enhanced Catalysis for Oxygen Reduction Reaction. *J. Am. Chem. Soc.* **2010**, *132*, 4996–4997. [CrossRef]
40. Vo, T.-G.; Hidalgo, S.D.S.; Chiang, C.-Y. Controllable electrodeposition of binary metal films from deep eutectic solvent as an efficient and durable catalyst for the oxygen evolution reaction. *Dalton Trans.* **2019**, *48*, 14748–14757. [CrossRef]
41. Liang, Y.; Liu, Q.; Asiri, A.M.; Sun, X.; He, Y. Nickel–iron foam as a three-dimensional robust oxygen evolution electrode with high activity. *Int. J. Hydrog. Energy* **2015**, *40*, 13258–13263. [CrossRef]
42. Biset-Peiró, M.; Murcia-López, S.; Fabrega, C.; Morante, J.-R.; Andreu, T. Multilayer Ni/Fe thin films as oxygen evolution catalysts for solar fuel production. *J. Phys. D Appl. Phys.* **2017**, *50*, 104003. [CrossRef]
43. Lima, C.G.; Silva, R.M.; Aquino, F.D.M.; Raveau, B.; Caignaert, V.; Cesário, M.R.; Macedo, D.A. Proteic sol-gel synthesis of copper doped misfit Ca-cobaltites with potential SOFC application. *Mater. Chem. Phys.* **2017**, *187*, 177–182. [CrossRef]
44. Silva, R.M.; Raimundo, R.A.; Fernandes, W.V.; Torres, S.M.; Silva, V.D.; Grilo, J.P.; Morales, M.A.; Macedo, D.A. Proteic sol-gel synthesis, structure and magnetic properties of Ni/NiO core-shell powders. *Ceram. Int.* **2018**, *44*, 6152–6156. [CrossRef]
45. Santos, J.R.; Loureiro, F.J.; Grilo, J.P.; Silva, V.D.; Simões, T.A.; Fagg, D.P.; Macedo, D.A. Understanding the cathodic polarisation behaviour of the misfit $[Ca_2CoO_{3-\delta}]q[CoO_2]$ (C349) as oxygen electrode for IT-SOFC. *Electrochim. Acta* **2018**, *285*, 214–220. [CrossRef]
46. Schneider, C.A.; Rasband, W.S.; Eliceiri, K.W. NIH Image to ImageJ: 25 Years of image analysis. *Nat. Methods* **2012**, *9*, 671–675. [CrossRef] [PubMed]
47. Bruker, A.X.S. *TOPAS V4: General Profile and Structure Analysis Software for Powder Diffraction Data*; User's Manual; Bruker AXS: Karlsruhe, Germany, 2009; Volume 72.
48. Brand, R.A. *Normos Programs, Normos Mössbauer Fitting Program*; University of Duisburg: Duisburg, Germany, 2002.
49. Gorter, E.W. Saturation Magnetization and Crystal Chemistry of Ferrimagnetic Oxides. 1954. Available online: https://www.lorentz.leidenuniv.nl/history/proefschriften/sources/Gorter_1954.pdf (accessed on 1 August 2023).
50. Ono, F.; Kittaka, T.; Maeta, H. Thermal expansion measurements in Fe-base invar alloys. *Phys. B+C* **1983**, *119*, 78–83. [CrossRef]
51. Chaudhuri, D.K.; Ravindran, P.A.; Wert, J.J. Comparative X-ray Diffraction and Electron Microscopic Study of the Transformation-Induced Substructures in the Iron-Nickel Martensites and Their Influence on the Martensite Properties. *J. Appl. Phys.* **1972**, *43*, 778–788. [CrossRef]
52. Lim, D.; Oh, E.; Lim, C.; Shim, S.E.; Baeck, S.-H. Bimetallic NiFe alloys as highly efficient electrocatalysts for the oxygen evolution reaction. *Catal. Today* **2019**, *352*, 27–33. [CrossRef]
53. Swartzendruber, L.J.; Itkin, V.P.; Alcock, C.B. The Fe-Ni (iron-nickel) system. *J. Phase Equilibria Diffus.* **1991**, *12*, 288–312. [CrossRef]
54. Yang, C.W.; Williams, D.B.; Goldstein, J.I. A revision of the Fe-Ni phase diagram at low temperatures (<400 °C). *J. Phase Equilibria Diffus.* **1996**, *17*, 522–531. [CrossRef]
55. Kubaschewski, O. *Iron-Binary Phase Diagrams*; Springer: Berlin/Heidelberg, Germany, 1982. [CrossRef]
56. Kurlyandskaya, G.; Bhagat, S.; Bagazeev, A.; Medvedev, A.; Ballesteros, A.; Beketov, I.; Safronov, A. Structure, magnetic and microwave properties of FeNi invar nanoparticles obtained by electrical explosion of wire in different preparation conditions. *J. Phys. Chem. Solids* **2016**, *98*, 255–262. [CrossRef]
57. Ping, T.; Das, T.K.; Jena, B.K. In-situ construction of porous Fe/Ni/Co-phosphide heterostructures with electron redistribution for the efficient water oxidation reaction. *Electrochim. Acta* **2023**, *459*, 142504–142514. [CrossRef]
58. Feng, B.; Hao, Y.; Chen, J.; Wang, H.; Zhong, C.; Yang, Y.; Yao, Y. Nanostructured NiFe (oxy)hydroxide fabricated on nickel foams by laser-induced water plasma for enhanced alkaline oxygen evolution reaction. *Appl. Surf. Sci.* **2023**, *622*, 156934–156943. [CrossRef]
59. Biesinger, M.C.; Payne, B.P.; Lau, L.W.M.; Gerson, A.; Smart, R.S.C. X-ray photoelectron spectroscopic chemical state quantification of mixed nickel metal, oxide and hydroxide systems. *Surf. Interface Anal.* **2009**, *41*, 324–332. [CrossRef]
60. Grosvenor, A.P.; Biesinger, M.C.; Smart, R.S.C.; McIntyre, N.S. New interpretations of XPS spectra of nickel metal and oxides. *Surf. Sci.* **2006**, *600*, 1771–1779. [CrossRef]
61. Nardi, K.L.; Yang, N.; Dickens, C.F.; Strickler, A.L.; Bent, S.F. Creating Highly Active Atomic Layer Deposited NiO Electrocatalysts for the Oxygen Evolution Reaction. *Adv. Energy Mater.* **2015**, *5*, 1500412. [CrossRef]
62. Silva, V.D.; Simões, T.A.; Loureiro, F.J.; Fagg, D.P.; Figueiredo, F.M.; Medeiros, E.S.; Macedo, D.A. Solution blow spun nickel oxide/carbon nanocomposite hollow fibres as an efficient oxygen evolution reaction electrocatalyst. *Int. J. Hydrog. Energy* **2019**, *44*, 14877–14888. [CrossRef]
63. Loureiro, F.J.; Souza, G.S.; Graca, V.; Araújo, A.; Grilo, J.P.D.F.; Macedo, D.; Fagg, D.P. Nickel-copper based anodes for solid oxide fuel cells running on hydrogen and biogas: Study using ceria-based electrolytes with electronic short-circuiting correction. *J. Power Sources* **2019**, *438*, 227041. [CrossRef]

64. Hoang, T.T.H.; Gewirth, A.A. High Activity Oxygen Evolution Reaction Catalysts from Additive Controlled Electrodeposited Ni and NiFe Films. *ACS Catal.* **2016**, *6*, 1159–1164. [CrossRef]
65. Bandal, H.A.; Jadhav, A.R.; Kim, H. Facile synthesis of bicontinuous Ni_3Fe alloy for efficient electrocatalytic oxygen evolution reaction. *J. Alloys Compd.* **2017**, *726*, 875–884. [CrossRef]
66. Franco, H.; Rechenberg, H.R. A Mossbauer study of the miscibility gap in iron-nickel Invar alloys. *J. Phys. F Met. Phys.* **1985**, *15*, 719–725. [CrossRef]
67. Ping, J.; Rancourt, D.; Dunlap, R. Physical basis and break down of hyperfine field distribution analysis in fcc Fe-Ni (5–70 at%Fe). *J. Magn. Magn. Mater.* **1992**, *103*, 285–313. [CrossRef]
68. Valderruten, J.; Alcazar, G.P.; Greneche, J. Study of Fe–Ni alloys produced by mechanical alloying. *Phys. B Condens. Matter* **2006**, *384*, 316–318. [CrossRef]
69. Arajs, S.; Miller, D.S. Paramagnetic Susceptibilities of Fe and Fe-Si Alloys. *J. Appl. Phys.* **1960**, *31*, 986–991. [CrossRef]
70. Keune, W.; Halbauer, R.; Gonser, U.; Lauer, J.; Williamson, D.L. Antiferromagnetism of fcc Fe thin films. *J. Appl. Phys.* **1977**, *48*, 2976–2979. [CrossRef]
71. Rodríguez, E.D.B.; Rodríguez, H.B.; Lozano, D.O.; Martínez, Y.A.R.; Alcázar, G.A.P. Mössbauer study of alloy $Fe_{67.5}Ni_{32.5}$, prepared by mechanical alloying. *Hyperfine Interact.* **2015**, *232*, 87–95. [CrossRef]
72. Yang, J.; Goldstein, J.I. Magnetic contribution to the interdiffusion coefficients in bcc (α) and fcc (γ) Fe-Ni alloys. *Met. Mater. Trans. A* **2004**, *35*, 1681–1690. [CrossRef]
73. Öner, Y.; Guler, A. Evidence of a Griffiths phase in a mixed compound of YFe_2 and YFe_3. *J. Appl. Phys.* **2013**, *113*, 17E141. [CrossRef]
74. Ubaid-Kassis, S.; Vojta, T.; Schroeder, A. Quantum Griffiths Phase in the Weak Itinerant Ferromagnetic AlloyNi1−xVx. *Phys. Rev. Lett.* **2010**, *104*, 066402. [CrossRef] [PubMed]
75. Araújo-Barbosa, S.; Morales, M.A. Nanoparticles of Ni1−Cu alloys for enhanced heating in magnetic hyperthermia. *J. Alloys Compd.* **2019**, *787*, 935–943. [CrossRef]
76. Cullity, B.D.; Graham, C.D. *Introduction to Magnetic Materials*, 2nd ed.; John Wiley & Sons, Inc.: Hoboken, NJ, USA, 2009.
77. Lourenço, A.D.A.; Silva, V.D.; da Silva, R.B.; Silva, U.C.; Chesman, C.; Salvador, C.; Simões, T.A.; de Macedo, D.A.; da Silva, F.F. Metal-organic frameworks as template for synthesis of Mn^{3+}/Mn^{4+} mixed valence manganese cobaltites electrocatalysts for oxygen evolution reaction. *J. Colloid Interface Sci.* **2021**, *582*, 124–136. [CrossRef] [PubMed]
78. Lian, J.; Wu, Y.; Zhang, H.; Gu, S.; Zeng, Z.; Ye, X. One-step synthesis of amorphous Ni–Fe–P alloy as bifunctional electrocatalyst for overall water splitting in alkaline medium. *Int. J. Hydrog. Energy* **2018**, *43*, 12929–12938. [CrossRef]
79. Jia, D.; Gao, H.; Zhao, J.; Xing, L.; Chen, X.; Huang, X.; Dang, R.; Wang, G. Self-templating synthesis of hollow NiFe hydroxide nanospheres for efficient oxygen evolution reaction. *Electrochim. Acta* **2020**, *357*, 136869. [CrossRef]
80. Silva, V.D.; Ferreira, L.S.; Simões, T.A.; Medeiros, E.S.; Macedo, D.A. 1D hollow MFe_2O_4 (M = Cu, Co, Ni) fibers by Solution Blow Spinning for oxygen evolution reaction. *J. Colloid Interface Sci.* **2019**, *540*, 59–65. [CrossRef]
81. Lv, Y.; Batool, A.; Wei, Y.; Xin, Q.; Boddula, R.; Jan, S.U.; Akram, M.Z.; Tian, L.; Guo, B.; Gong, J.R. Homogeneously Distributed NiFe Alloy Nanoparticles on 3D Carbon Fiber Network as a Bifunctional Electrocatalyst for Overall Water Splitting. *ChemElectroChem* **2019**, *6*, 2497–2502. [CrossRef]
82. Anantharaj, S.; Ede, S.R.; Karthick, K.; Sankar, S.S.; Sangeetha, K.; Karthik, P.E.; Kundu, S. Precision and correctness in the evaluation of electrocatalytic water splitting: Revisiting activity parameters with a critical assessment. *Energy Environ. Sci.* **2018**, *11*, 744–771. [CrossRef]
83. McCrory, C.C.L.; Jung, S.; Peters, J.C.; Jaramillo, T.F. Benchmarking Heterogeneous Electrocatalysts for the Oxygen Evolution Reaction. *J. Am. Chem. Soc.* **2013**, *135*, 16977–16987. [CrossRef]
84. Wang, J.; Gan, L.; Zhang, W.; Peng, Y.; Yu, H.; Yan, Q.; Xia, X.; Wang, X. In situ formation of molecular Ni-Fe active sites on heteroatom-doped graphene as a heterogeneous electrocatalyst toward oxygen evolution. *Sci. Adv.* **2018**, *4*, eaap7970. [CrossRef]
85. Song, F.; Hu, X. Exfoliation of layered double hydroxides for enhanced oxygen evolution catalysis. *Nat. Commun.* **2014**, *5*, 4477. [CrossRef]
86. Qi, J.; Zhang, W.; Xiang, R.; Liu, K.; Wang, H.; Chen, M.; Han, Y.; Cao, R. Porous Nickel–Iron Oxide as a Highly Efficient Electrocatalyst for Oxygen Evolution Reaction. *Adv. Sci.* **2015**, *2*, 1500199. [CrossRef]
87. Yu, X.; Zhang, M.; Yuan, W.; Shi, G. A high-performance three-dimensional Ni–Fe layered double hydroxide/graphene electrode for water oxidation. *J. Mater. Chem. A* **2015**, *3*, 6921–6928. [CrossRef]
88. Zhang, X.; Xu, H.; Li, X.; Li, Y.; Yang, T.; Liang, Y. Facile Synthesis of Nickel–Iron/Nanocarbon Hybrids as Advanced Electrocatalysts for Efficient Water Splitting. *ACS Catal.* **2016**, *6*, 580–588. [CrossRef]
89. Wu, L.-K.; Zhu, Y.-X.; Liu, M.; Hou, G.-Y.; Tang, Y.-P.; Cao, H.-Z.; Zhang, H.-B.; Zheng, G.-Q. Ultrafast fabrication of amorphous bimetallic hydroxide layer on nickel nanocones array for oxygen evolution electrocatalyst. *Int. J. Hydrog. Energy* **2019**, *44*, 5899–5911. [CrossRef]
90. Gao, X.; Long, X.; Yu, H.; Pan, X.; Yi, Z. Ni Nanoparticles Decorated NiFe Layered Double Hydroxide as Bifunctional Electrochemical Catalyst. *J. Electrochem. Soc.* **2017**, *164*, H307–H310. [CrossRef]
91. Si, S.; Hu, H.-S.; Liu, R.-J.; Xu, Z.-X.; Wang, C.-B.; Feng, Y.-Y. Co–NiFe layered double hydroxide nanosheets as an efficient electrocatalyst for the electrochemical evolution of oxygen. *Int. J. Hydrog. Energy* **2020**, *45*, 9368–9379. [CrossRef]

92. Liu, Z.; Tang, B.; Gu, X.; Liu, H.; Feng, L. Selective structure transformation for NiFe/$NiFe_2O_4$ embedded porous nitrogen-doped carbon nanosphere with improved oxygen evolution reaction activity. *Chem. Eng. J.* **2020**, *395*, 125170. [CrossRef]
93. Hu, J.; Zhu, S.; Liang, Y.; Wu, S.; Li, Z.; Luo, S.; Cui, Z. Self-supported Ni_3Se_2@NiFe layered double hydroxide bifunctional electrocatalyst for overall water splitting. *J. Colloid Interface Sci.* **2021**, *587*, 79–89. [CrossRef]
94. Li, S.; Liu, J.; Duan, S.; Wang, T.; Li, Q. Tuning the oxygen evolution electrocatalysis on NiFe-layered double hydroxides via sulfur doping. *Chin. J. Catal.* **2020**, *41*, 847–852. [CrossRef]
95. Ferreira, L.S.; Silva, T.R.; Santos, J.R.; Silva, V.D.; Raimundo, R.A.; Morales, M.A.; Macedo, D.A. Structure, magnetic behavior and OER activity of $CoFe_2O_4$ powders obtained using agar-agar from red seaweed (Rhodophyta). *Mater. Chem. Phys.* **2019**, *237*, 121847. [CrossRef]
96. Swierk, J.R.; Klaus, S.; Trotochaud, L.; Bell, A.T.; Tilley, T.D. Electrochemical Study of the Energetics of the Oxygen Evolution Reaction at Nickel Iron (Oxy)Hydroxide Catalysts. *J. Phys. Chem. C* **2015**, *119*, 19022–19029. [CrossRef]